Analysis of the relation between phase transformation kinetics and energy dissipation in vanadium microalloyed steels

Ewoud van Rhee

MSc Thesis

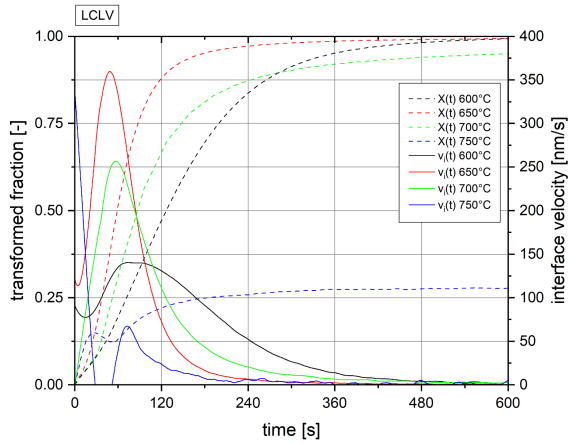

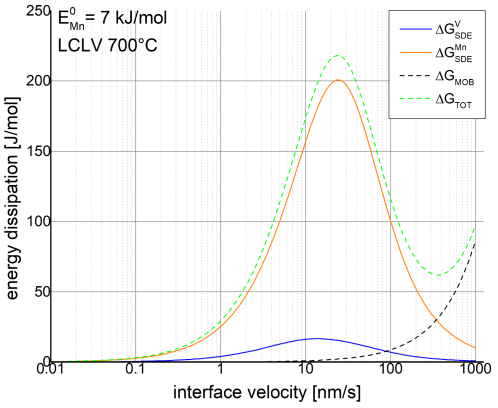

TU Delft

Analysis of the relation between phase transformation kinetics and energy dissipation in vanadium microalloyed steels

Thesis report
by
Ewoud van Rhee

to obtain the Master of Science degree in Materials Science and Engineering at the Delft University of Technology, to be defended publicly on Tuesday May 12th, 2026 at 15:15 hr.

Thesis committee:
Dr. Ir. Erik Offerman
Dr. Hossein Beladi
Dr. Pina Mecozzi
MSc. Amir Sabet Ghorabaei

Student number:
4474546

Faculty of Materials Science & Engineering

TU Delft

Acknowledgements

This thesis marks the conclusion of obtaining my masters degree at the Delft University of Technology. I greatly enjoyed the many topics on metals which were treated at the faculty of Materials Science and Engineering. Being able to connect experimental and theoretical modeling work as a final task gave great enjoyment.

I would like to thank my supervisors Dr. Ir. Erik Offerman and Dr. Pina Mecozzi for their support during my thesis. The lengthy discussions we had on various topics were greatly educational and exceptionally useful to the project.

I would like to thank my mother, for her patience and support during this time, and my father, who sadly would never get the chance to see me graduate and grow further, but who inspired and motivated me greatly to start and finish my journey at TUDelft.

Abstract

Microalloyed steels strengthened by precipitates nucleated during the austenite (γ) to ferrite (α) phase transformation can provide steel producers with a new type of High Strength Low Alloy (HSLA) steel suitable for increasing demands for their properties. To better understand the conditions at the migrating α/γ interface, which can lead to said precipitation, the kinetics of the phase transformations are investigated.

Three different microalloyed steels with the same amount of manganese and varying amounts of carbon and vanadium are analysed on four different annealing temperatures. Experimental data on the phase transformation kinetics is obtained through dilatometry. A quantitative solute drag model is developed and tested on the quaternary alloys to obtain data on energy dissipation due to segregation of the substitutional elements. A theory is postulated to relate the experimental data and related obtained interface velocities to the modelling results.

Experimental results vary greatly, but at medium (650°C) to high (750°C) annealing temperatures an increase of vanadium and carbon content leads to a slower transformation compared to the alloy with lower concentrations of said elements.

Modelling results indicate that energy dissipation due to vanadium is minimal, especially relative to that of manganese. This means that observed changes in transformation dynamics for the alloys with changing vanadium and carbon content have to be understood in terms of vanadium-carbide precipitation behaviour and related elemental consumption, and not in energy dissipation due to vanadium segregation.

Contents

1. Introduction

1.1 Industrial relevancy

Steels are one of the most used materials on the globe. The wide versatility and usefulness of their properties make them highly applicable in many industrial sectors, and the relative abundance of the element iron in the earth's crust and the ease of refining drives their costs down.

Development to improve the quality of steels is a continuous process. Industrial sectors are always looking to optimize their products and processes by using more optimal materials. Steel makers, whose customer demands are increasing, must follow this trend amidst high competition. An example of such an important sector is the automotive industry, where producing components with less material (thus reducing weight) while still retaining the required mechanical and physical properties is of paramount importance.

Steels are often classified by means of composition and processing information. Another important classification method is by the strength of the steel. High Strength Low Alloy (HSLA) and Advanced High Strength Steels (AHSS) are umbrella terms for steels with yield tensile strengths greater than 500 MPa and 700 MPa respectively. The main difference between conventional HSLA steels and AHSS is their microstructure. Conventional HSLA steels are single-phase ferritic steels with a potential for some phase-mixture pearlite in C-Mn steels. AHSS are primarily steels with a multiphase microstructure containing one or more phase and phase-mixtures other than ferrite, pearlite, or cementite – for example martensite, bainite, austenite, and/or retained austenite in quantities sufficient to produce unique mechanical properties.

Generally, an issue with increasing strength of steels is the general loss of ductility and formability, this is often due to the large mismatch of strength between martensite and ferrite, the latter of which then suffers high stress concentrations. Car bodies, e.g. hoods are stamped out of sheet steel and are subjected to high levels of elastic and plastic deformation. These high strains can lead to cracking in conventional AHSS, which is unacceptable. Another typical downside of some AHSS is their (high) usage of expensive alloying elements.

A potential new HSLA or AHSS candidate whose primary formation mechanisms are the subject of many research, can be microalloyed ferritic steels hardened by nano-sized carbo(nitride) precipitates, which are formed during the consecutive thermomechanical processing (TMP) or during the austenite to ferrite phase transformation during continuous casting. These steels would combine a relative ductile ferrite matrix which benefits the formability such as hole-expansion capability, with the hard and very tiny carbo(nitride) precipitates for a substantial increase in strength. They would be strong while remaining suitable for high elastic deformation and be microalloyed and thus require relatively low amounts of expensive alloying elements.

There are two main methods to induce these nano-carbides to precipitate during isothermal holding at a temperature of ferrite and alloy carbide stability into the steel, a process known as precipitation hardening. The first, and most conventionally utilised manner, is from supersaturated ferrite (or martensite) during the aforementioned TMP, namely the quench and

tempering process. Here, precipitates are formed randomly throughout the ferritic matrix, and is as such dubbed random-precipitation (RP). The second way is associated with the austenite (γ) to ferrite (α) phase transformation, where carbides precipitate periodically in regular and (somewhat) parallel structures or bands on the migrating γ-α interface, a process known as interphase-precipitation (IP). The occurrence of one of the two different processes thus depends on whether the holding temperature is reached from a higher or lower temperature.

1.2 Interphase precipitates

As mentioned earlier, interphase precipitation is the phenomenon of the nucleation of carbides in steel during the austenite to ferrite phase transformation. These carbides are precipitated in regularly spaced bands or sheets and according to some authors [1] in aligned fibres. At first it was proposed that the carbides would nucleate on dislocations that originated due to strains at the phase transformation. Afterwards it was suggested that the precipitates nucleated on the phase boundary itself, which led to its name. In the mid 70's micrographs showed that in chromium alloyed steels the regularly spaced bands of carbides occurred along the planar boundary between γ and α. This suggested that the spaced sheets were created on the terrace in the γ-α interfaces. Afterwards many other carbides have been shown to be formed due to IP, eg., NbC, Mo_2C, V_4C_3 and $Cr_{23}C_6$ and have different morphologies including disk-shaped, circular and needle-like [2].

It has been noted that the precipitated MC carbides often have the B1 (NaCl) crystal structure and follow a single variant of the Baker-Nutting orientation relationship (B-N OR, $(100)_\alpha//(100)_{MC}, [001]_\alpha//[01\bar{1}]_{MC}$) between the carbides and the main ferrite matrix, contrary to precipitates formed in RP. The selection of a specific variant is evidence for the precipitation on the interface since free energy is minimised [3]. ***Figure 1.1.*** visualises a variant of this specific OR between the MC (B1) precipitates and the α (bcc) matrix. This variant minimises the angle between low energy planes of the precipitates and the α/γ interface that can reduce the free energy for the growth kinetics of IP by enhancing interfacial diffusion [4].

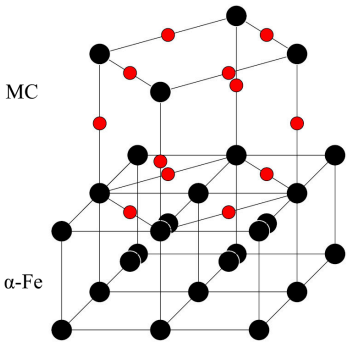

Fig. 1.1. Visualisation of the Baker-Nutting orientation relationship, adapted from [5].

During TMP, parameters such as cooling rate, isothermal temperature, strain level and cooling rate influence the interphase behaviour. These parameters affect the velocity of the interface migration and the diffusion of the alloying elements which leads to different morphologies and properties of the precipitates such as size, number density and volume fraction. This subsequently leads to varying strengthening behaviour.

Extensive research and characterisation into these steels has been active only relatively recently, due to developments in advanced characterisation methods which enable measurement and analysis of nanometer sized particles on the atomic scale, which previously has been impossible. Difficulties in characterisation are the extremely small size (nanometer range) of the precipitates, the presence of dislocations in α and the ferromagnetic nature of α. In addition, IP can only be seen by electron microscopy when the electron beam is roughly parallel to the precipitation plane, which otherwise suggests that precipitation has been random [6].

A great potential advantage of IP steels is that it can occur during continuous cooling (CC), and hence no further expensive and time consuming ageing treatments would have to be performed as is the case with conventional precipitation hardened metals. A resistance to coarsening has been found by precipitates formed by IP, thus maintaining a high strength contribution throughout the production process. This was verified by a low hardness decrease of the steel after isothermal holding at conventional coarsening temperatures for (Ti,Mo)C precipitates. This would essentially entail that a second generation AHSS with the costs of HSLA steels could be manufactured.

2. Theoretical Background

This chapter provides a brief overview of the austenite-to-ferrite transformation and the associated energy dissipation processes, with particular emphasis on the solute drag effect.

2.1 The austenite to ferrite phase transformation

Steel has multiple allotropes which are stable under varying conditions. In practical sense, pressure is kept constant which makes the dependance of phase stability rely on temperature and chemical composition. At the Ae3 point (910 °C for pure iron) steel transforms from ferrite (α) to austenite (γ) when heated up. This phase transformation is accompanied by a volume change of approximately 1-3% due to the differences in packing densities of the crystal structures. Although the fcc structure is more densely packed, it has larger interstice sites which allow a higher solubility of solutes, which is relevant for the processing mechanics.

The Ae3 phase transformation is reconstructive when transformation kinetics are slow enough to prevent bainite or martensite, this means all bonds are broken and the atoms are rearranged in an alternative pattern. It is the diffusion of atoms which leads to the formation of a new crystal structure, which indicates the dependency of transformation temperature.

In order to qualitatively and quantitatively model the phase transformation a description of the interface between α and γ is a necessity. Essentially, three main types of interface descriptions can be ascertained; the classical sharp interface with no width, the interface with a finite width and the interface where the width is not fixed a-priori known as the diffuse interface. The choice of the interface is predominantly based on the ease of encompassing physical processes both in the bulk as at the interface. An important process is the dissipation of the chemical driving force during the transformation, and whether this is done by elemental diffusion or by friction within the interface.

Depending on the assumed interface model, the transformation can in extremities be considered to be either (i) diffusional controlled, or (ii) interfacial controlled. For the diffusional controlled transformation corresponding to a sharp interface, the driving force of transformation is fully consumed by partitioning and long range bulk diffusion when the transformation kinetics are slow, and these are then the rate limiting steps. It is assumed that the reconfiguration of a new crystal structure upon the passage of an interface is fast enough to not play a significant role in the overall kinetics [7]. The other case, namely interfacial controlled transformation assumes the bulk diffusion is infinitely fast and there is no change in composition across the interface. All driving force is consumed by structural rearrangement and friction at the interface and this friction force is assumed to be proportional to the rate of migration.

Since neither the diffusivity as the interface mobility are inexhaustible, a mixed mode is assumed to be the case, which combines elements from diffusional and interfacial control. Here both bulk diffusion of carbon from α into γ and the change at the phase interface consumes driving force. A good review paper on the austenite to ferrite phase transformation is recommended [8].

There are two main practical models for solute redistribution along the γ/α interface for a Fe-C-X alloy, namely the (i) negligible-partitioning local equilibrium (NPLE) and (ii) para-equilibrium (PE) condition. The NPLE condition at the interface is upheld by diffusion of

atoms at the interface and results in the creation of a solute spike due to local partitioning of substitutional solutes. The PE mode implies that the substitutional solutes are completely immobile, even as the interface glides through/across them. The velocity of the interface is assumed to be faster than the diffusion of substitutional elements. These two modes provide theoretical limits for solute concentrations which may be achieved during the α transformation [9]. Both NPLE and PE conditions have been verified to be more accurate to predict the transformation kinetics for different γ/α OR, and it is suggested that interface velocity and transformation temperature can influence the mode of operation [10].

Fig. 2.1. presents schematic phase diagrams and compositional profiles for an Fe–C–Mn steel alloy at 700 °C, illustrating the transformation conditions under non-partitioning local equilibrium and paraequilibrium. The isothermal section of the Fe–C–Mn phase diagram is shown in **Fig. 2.1(a)**. [7].

In **Fig. 2.1(a)**, the zero-partition line divides the α/γ two-phase region into two distinct domains. For alloys whose composition lies above the zero-partition line, the transformation requires partitioning of substitutional alloying elements, such as Mn, between ferrite and austenite. These transformation conditions are referred to as partitioning local equilibrium (PLE). In this case, substitutional elements redistribute across the migrating interface in order to satisfy full local equilibrium. However, such conditions are rarely sustained in practice because substitutional diffusion is relatively slow compared to the transformation rate. Therefore, PLE conditions are not considered further in this discussion.

For alloys with compositions below the zero-partition line, the transformation proceeds under NPLE conditions. In this regime, substitutional elements such as Mn do not significantly redistribute between the phases. Instead, a narrow solute spike develops at the migrating ferrite/austenite interface, as illustrated in **Fig. 2.1(b)**. This spike forms because Mn diffusion is limited and cannot redistribute over large distances during the transformation. NPLE conditions typically occur in alloys with relatively low solute concentrations and are maintained at moderate transformation rates. The carbon distribution corresponding to NPLE conditions is shown schematically in **Fig. 2.1(c)**.

In contrast, under paraequilibrium conditions, the interface migration rate is faster than the diffusion rate of substitutional elements. As a result, substitutional atoms such as Mn remain effectively immobile during the transformation and maintain the same concentration in both phases. In this scenario, the Mn concentration profile follows a paraequilibrium tie-line, as illustrated in **Fig. 2.1(d)** and no Mn spike develops at the interface.

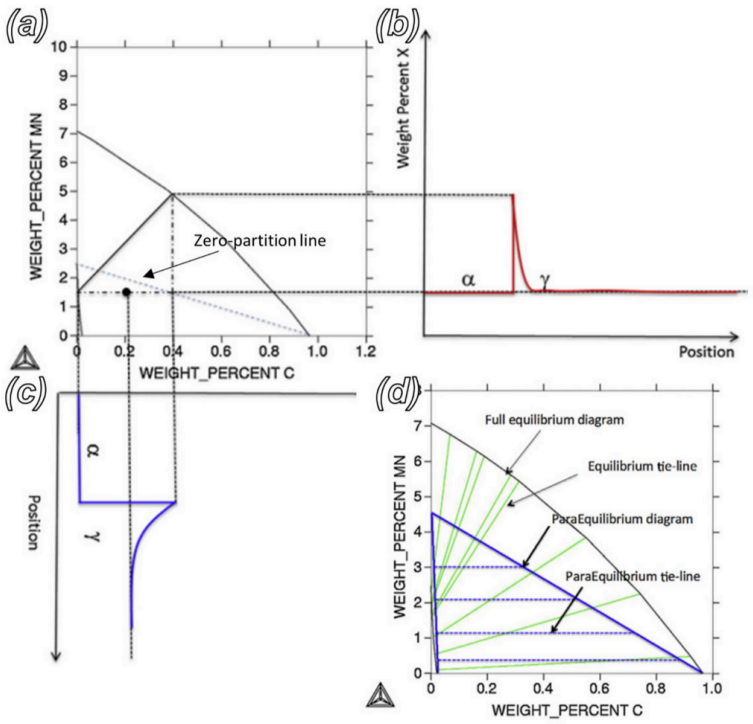

Fig. 2.1. Schematic NPLE and PE phase diagrams and local compositional profiles illustrating the local conditions at the ferrite/austenite migrating interface of the Fe–C– Mn system at 700 °C: (a) The transformation is accompanied by Mn spike and is controlled by the NPLE conditions; (b) Mn compositional profile corresponding to NPLE conditions; (c) C compositional profile corresponding to NPLE conditions; (d) The transformation proceeds without Mn spike and is controlled under PE conditions. [7]

Although substitutional elements remain fixed during PE transformation, carbon remains highly mobile and can redistribute to maintain equilibrium between the phases. Consequently, a carbon concentration spike develops at the interface, corresponding to the intersection between the paraequilibrium tie-line and the α+γ / γ boundary in the paraequilibrium phase diagram. Notably, the carbon spike formed under PE conditions is larger than that observed under NPLE conditions, as illustrated in **Fig. 2.1(d)**.

A challenge associated with both PE and NPLE descriptions lies in the composition ranges where the two models predict significantly different transformation rates. In reality, substitutional atoms must undergo reconstructive rearrangements during the γ to α transformation, meaning that their complete immobility, as assumed in the PE model, may not be physically realistic. Conversely, the NPLE model predicts a solute spike with a width on the order of the interatomic distance, which raises questions regarding its physical validity as well.

Despite these limitations, the PE and NPLE models remain useful because they define theoretical limiting cases for solute redistribution during phase transformation. Actual transformations in steels may occur somewhere between these two extremes, depending on factors such as temperature, alloy composition, and interface migration rate.

Returning to the mixed-mode, models for binary alloys have been developed such as [11] which include a diffusional as an interfacial approach. This methodology converges to the respective approach depending on whether the diffusion coefficient or interface mobility is dominant. Yet for ternary or more complex systems the mixed-mode models must and have been

adapted to include additional assumptions. In general, a mixed-mode model must balance the driving force with the dissipation of energy while including a mass balance at the interface.

Interphase precipitation takes place at low mobility interfaces, which need more driving force in order to be moved. This leads to interface characteristics dominating over diffusional characteristics, until a solute flux is required for precipitate growth. Since the diffusivity of microalloying elements tends to be much greater in α than in γ, the interface can be expected move along the solute depletion in the ferrite, since the trans interface diffusivity is expected to be much greater than in bulk, and can be estimated as an average function of the diffusivities in α and γ. With the mobility of substitutional solutes in mind, it would seem logical to assume a NPLE condition is required for interphase precipitation to be able to occur. However, in the early stages when the interface velocity is very fast, the NPLE condition fails to provide meaningful results, and a PE mode is more suited. Hence, a transition from PE to NPLE mode during the phase transformation could exist, and has been the subject of various research to develop so-called transition models. Solute-drag based models are in fact transition models themselves.

2.2 The solute drag approach

Experiments in recrystallisation (rex.) have shown the existence of diffusional drag induced by solutes on grain boundary motion. The segregation of these substitutional elements at grain boundaries has shown to lead to changes in the rex. temperatures of deformed steels. This can be understood in terms of the association of atoms with moving grain boundaries, where the solute-boundary interaction energy can be negative or positive, depending on whether there is adsorption or desorption respectively of the solute at the boundary. In particular cases, the solute atoms are expected to be dragged along (negative) or pushed ahead (positive) of the boundary, reducing its rate of migration.

This interaction between the less-mobile solutes and the migrating boundary was thus proposed to be akin to a type of dragging mechanic. It was noted that the earlier formulated analysis of solute drag in the context of grain boundary migration cannot directly be applied to phase transformations [12].

However, the idea of this solute drag was naturally expanded to phase transformations as well. The solute drag can be considered as a force when balancing the forces acting upon a moving interface [13]:

$$P_{solute\ drag} + P_{friction} + P_{\sigma} = 0 \quad (2.1)$$

The first term is the net force caused by the attraction between solute atoms and the interface. It is the force by which the migrating interface drags locally segregated solutes with it [13]. The solute atoms resist the migration by exerting an equal but opposite force on the interface. The second term is the inherent resistance to migration, coined intrinsic drag or the friction of a migrating interface. The final term exists if the interface is curved and inhibits interfacial energy caused by this curve. Effects of deformation of untransformed austenite, which will be discussed later, will also be inhibited in this P_{σ} term.

When multiplying this equation with the molar volume, the first term now represents the dissipation of Gibbs free energy for each mole of atoms, and the second term represents the dissipation by friction:

$$P_{solute\ drag}V_m + P_{friction}V_m + P_\sigma V_m = 0 \quad (2.2)$$

Another approach is based upon the driving force of migration of the interface. The chemical driving force D_{chem} can be evaluated from the difference in chemical potentials at the sides of the interface and the net composition of the material passed by the interface under steady-state conditions [13]:

$$D_{chem} = \sum x_i^{tr}\left(\mu_i^{\gamma/\alpha} - \mu_i^{\alpha/\gamma}\right) \quad (2.3)$$

The chemical driving force must be equal to the sum of the kinks of Gibbs free energy. Under steady-state when the composition profile inside the interface moves with the interface without changing, the following equation can be written [13]:

$$D_{chem} = \Delta G_{diff} + \Delta G_{friction} + P_\sigma V_m \quad (2.4)$$

The first term on the right hand side of the equation represents the dissipation of Gibbs free energy due to diffusion of solutes being dragged along with the moving interface. The second term is the dissipation due to friction and is identical to $P_{friction}V_m$.

These two different approaches are equivalent if:

$$P_{solute\ drag}V_m = \Delta G_{diff} - D_{chem} \quad (2.5)$$

The solute drag for grain boundary migration was evaluated by Lücke and Stüwe [14] and Cahn [15]. Cahn predicted that the effects of drag occurred in two different modes, a (i) high velocity, low driving force and a (ii) low-velocity, high driving force mode. It was shown that the grain boundary migration velocity may not be linearly proportional to the actual driving force when solutes are segregated at the boundaries, which depends on migration kinetics, driving force and concentration. Hillert and Sundman [16] used the free energy dissipation approach, expanded the theory to phase transformations and came to similar results. He argued that the work put into the movement of a boundary in order to overcome the solute drag, must be dissipated by the diffusion of the solute taking place as a result of the boundary movement [7]. This dissipation approach was expanded upon by Purdy and Brechet [17], but problems arose when the chemical driving force was forced to be introduced into the solute drag treatment. In addition, their approach has physical assumptions with respect to segregation which may not be based on reality. Also it was claimed that the solute drag approach and dissipation approach lead to different results, contrary to Hillert and Sundman's conclusions. Odqvist et al. [18] showed that Purdy and Brechet had made a mistake considering the compared driving force. Later, Enemoto [19] developed their model further by including the variation of thermodynamic interaction between carbon and the alloying elements across the interface surface where cosegregation of both carbon as the substitutional solutes are considered. A variation of the Hillert-Sundman approach was then again considered by Odqvist et al. [20] and Hillert [13]**.** A common problem or trend of all these mix-mode transition approaches however, is their dependence on critical interfacial properties, such as trans-interface diffusivities, which are often unknown. As such, average values are used, or the models are used to fit data.

3. Experimental

In this chapter the methods and materials of the performed experiments will be presented.

3.1 Dilatometry

3.1.1 Sample creation

Three different cast and rolled microalloyed steels were analysed. The primary investigated elemental contributions are carbon, vanadium and manganese. The amount of carbon and vanadium are varied between the alloys while the content of the remaining elements is held at constant level. The chemical composition of the steels is provided in **Tab. 3.1**. The three analysed steels have a baseline low-carbon no-vanadium, a low-carbon low-vanadium and a high-carbon high-vanadium composition and are referred to respectively as BASE, LCLV and HCHV.

Tab. 3.1.
Chemical composition of used alloys

Sample		C	V	Mn	Si	S	Al	Fe
BASE	wt. %	0.068	0.001	1.792	0.018	0.0008	0.022	bal.
LCLV	wt. %	0.068	0.285	1.790	0.008	0.0013	0.035	bal.
HCHV	wt. %	0.138	0.609	1.790	0.011	0.0012	0.036	bal.

Rectangular shaped dilatometry specimens of 2.5 x 5 x 10 mm^3 were created. The samples were created in the same manner for all of the provided steels. Sheets of ca. 2.5 mm thick were provided. These sheets were milled flat at upper and lower surfaces to clean up the rough texture. Due to slight curvature in the sheets, likely due to internal stresses, they were placed and milled on a magnetic clamping table to keep the sheet surface perpendicular to the mill-axis. Once unclamped, curvature of the sheet decreased substantially after milling, indicating a relief of internal stresses.

From the milled sheets dilatometry samples with dimensions of ca. 10 mm by 5 mm were cut using a heavy duty press brake. The sample length axis is parallel to the dilatometry measuring axis, i.e. the sample is clamped and measured along its length. To find out if any effects of rolling anisotropy would affect the dilatometry measurements, samples with their length both along the steel's rolling and transverse directions were made. **Fig. 3.1.** schematically indicates the sample creation from the steel sheets with their respective orientation axis.

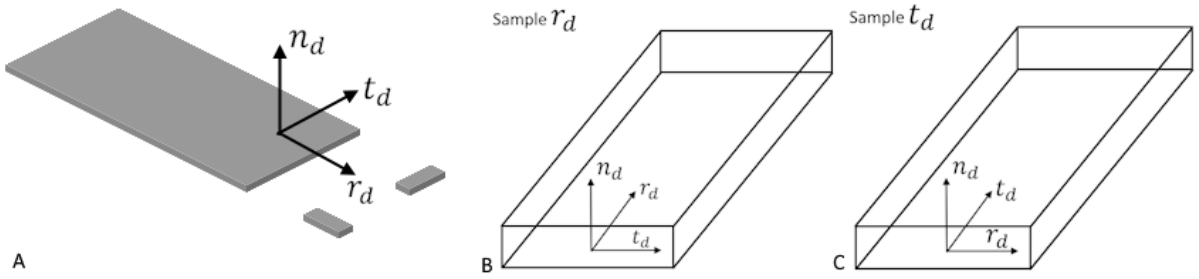

Fig. 3.1. Schematic representation of sample creation and orientation with respect to original slab with: (a) The steel slab and its coordinate system including the two sample types; (b) sample r_d with the original coordinate system; (c) sample t_d with the original coordinate system.

Final sample dimensions varied a maximum of $\pm$ 0.2 mm from baseline dimensions. Effects on heat distribution during dilatometry due to this varying sample size was deemed negligible. Each sample was measured up to a five digit significance in units of mm and those values were used as input in the dilatometry measuring control software.

3.1.2 Dilatometry methodology

In order to determine the phase transformation kinetics of the steels, dilatometry experiments were carried out. A TA DIL 805 A/D/T dilatometer was used. One S-type platinum thermocouple per sample was spot welded on the middle of the surface to measure and control the temperature during the cycle. The change in length of the specimen is recorded as a function of temperature and the resulting dilatometry data is used to study the phase transformation kinetics for each alloy. The heating cycle is schematically shown in **Fig. 3.2.** Samples were austenised in a vacuum of at least 10^{-4} mbar at 1100°C for 5 minutes and then cooled with helium gas at a rate of 15°C/s towards varying annealing temperatures T_a shown in **Tab. 3.2.** and then held for varying annealing durations t_a dependent on the temperature. The austenisation temperature was chosen as the high-end used in previous research [21] which lies above the expected precipitate dissolution temperature.

Tab. 3.2.
Used annealing temperatures and corresponding durations

Annealing temperature T_a [°C]	Annealing duration t_a [hr]
600	1
650	1
700	4 and 16
750	4

Samples were also austenised and then immediately quenched for the determination of the prior austenite grain size (PAGS).

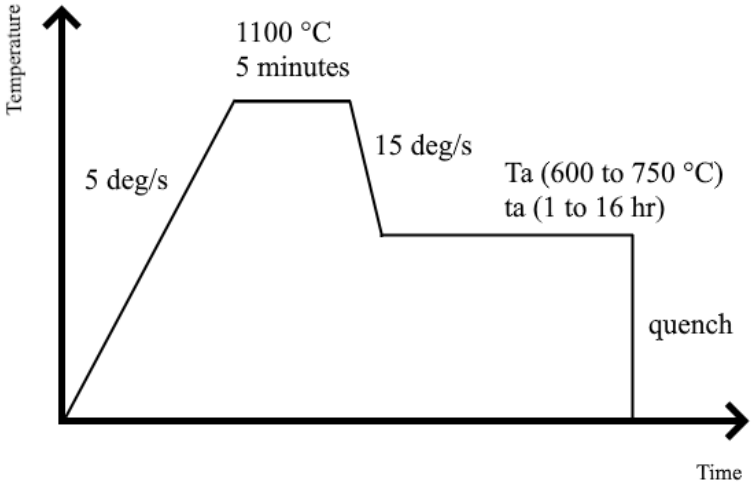

Fig. 3.2. Schematic representation of thermal cycles applied in the dilatometer.

3.1.3 Estimation of interface velocity

The unedited dilatometry data is unsuited for the direct estimation of the interface velocity and only the annealing part is desired. The onset of phase transformation, and the corresponding related data, is chosen as the moment at which the measured temperature is within 0.5°C of T_a after cooling down from the austenisation temperature. **Fig. 3.3.** shows this selected section for the LCLV 700°C sample. In addition it can be observed that the change in length starts at 0 µm, the actual value (from the raw data) at the selected onset of annealing is subtracted from the total change in length. This is done in order that the derivation calculation functions correctly.

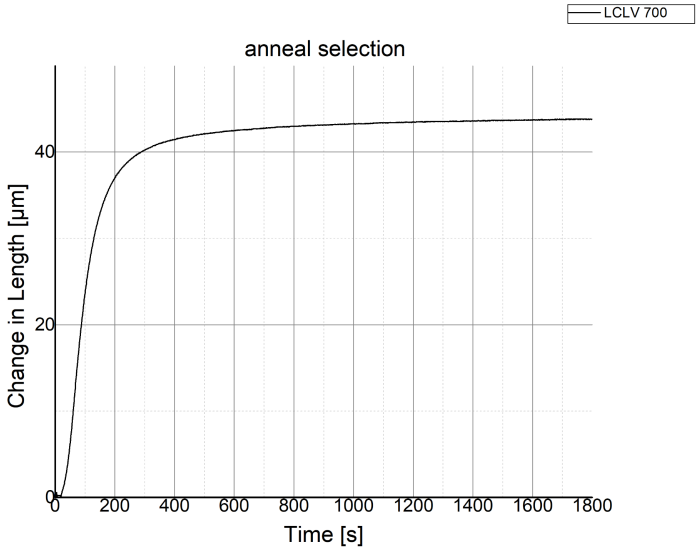

Fig. 3.3. Selected section of annealing of LCLV 700°C, starting at 0.5°C from 700°C.

In some dilatometry data, especially at the higher temperatures of 750°C, small fluctuations were observed right when reaching the annealing temperature. In these cases, the onset of

annealing was still selected before these fluctuations evened out. It is not clear what caused these dips. It was assumed and estimated that these were not caused by the transformation already starting during the cooling stage from soaking to annealing temperature, since these artifacts were less pronounced at lower annealing temperatures, where the driving force for transformation is higher and a premature start of transformation is more likely to happen. It is guessed that these had more to do with improper heat distribution throughout the sample.

The overall interface velocity v_i can be related by the increase of ferrite fraction f_a assuming a planar interface by using the relation:

(3.1) $$df_a = \frac{v_i}{r_\gamma} dt$$

(3.2) $$v_i = \frac{df_a}{dt} r_\gamma$$

Here r_γ is half the prior austenite grain size.
The increase of ferrite fraction, or transformed fraction of austenite $X(t)$ can be calculated from the dilatometry dilation data by using the lever rule:

(3.3) $$f_a = X(t) = \frac{\Delta L(t) - \Delta L0}{\Delta L\infty - \Delta L0}$$

And thus:

(3.4) $$df_a = \frac{dX(t)}{dt}$$

Here the baseline ΔL_0 is chosen to be the average of the first 10 entries to reduce the artifacts due to thermal fluctuations of the dilatometer, and ΔL_∞ is simply the last data entry of the selected annealing section:

(3.5) $$\Delta L_0 = \frac{1}{10} \sum_{i=1}^{10} L(t_i)$$

(3.6) $$\Delta L_\infty = L(t_{last})$$

For the lower annealing temperatures it could be assumed that the phase transformation is fully completed at moment of quenching, hence $X(t)$ would range from 0 to 1. Analysis of optical micrographs made of the annealed microstructure of samples annealed at 650°C verifies this assumption, showcased in **Fig. 3.4**. All optical micrographs were made with a VHX 7000N microscope. Here, a fully ferritic microstructure can be observed after quenching, verifying a complete transformation and no formation of martensite upon final quench.

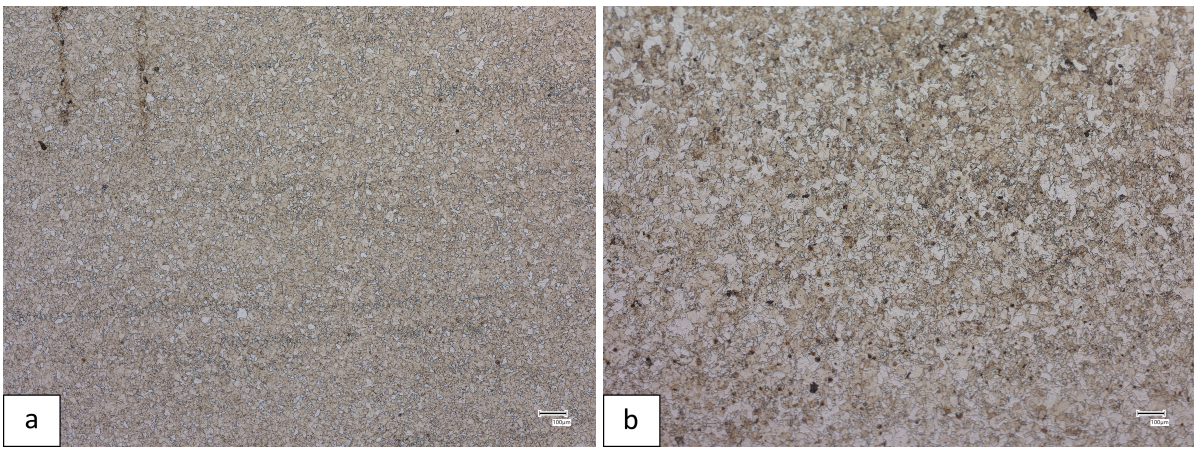

Fig. 3.4. Observed microstructure in (a) LCLV and; (b) HCHV alloys annealed at 650°C.

At higher temperatures, this assumption is likely to be invalid. Hence, it was chosen to roughly estimate the transformed fractions by analysing the dilation-temperature plots, for all temperatures. Here a quasi lever rule is used by elongating the linear parts of the extension graphs until they cross the y-axis. This is shown in **Fig. 3.5**. Then, the fraction of vertical distance between crosspoints estimates what fraction of untransformed austenite remains at the onset of quenching. The fraction of transformed austenite is then estimated as:

$$X_{estimated} = \frac{l_t}{l_u + l_t} \quad (3.7)$$

The resulting estimated and used transformed fractions are compiled in **Tab. 3.3.** Note that this estimation is crude, and takes great assumptions with regards to a non-existent austenitic temperature extension coefficient at low temperatures. Nonetheless, it is assessed that this gives a reasonable estimate. It has to be noted that using this methodology, for transformation at 750°C, a higher transformed fraction is obtained than in previous literature in a similar alloy [21], where only very small fractions of transformed ferrite were found using optical methods. This is especially the case for the HCHV alloy.

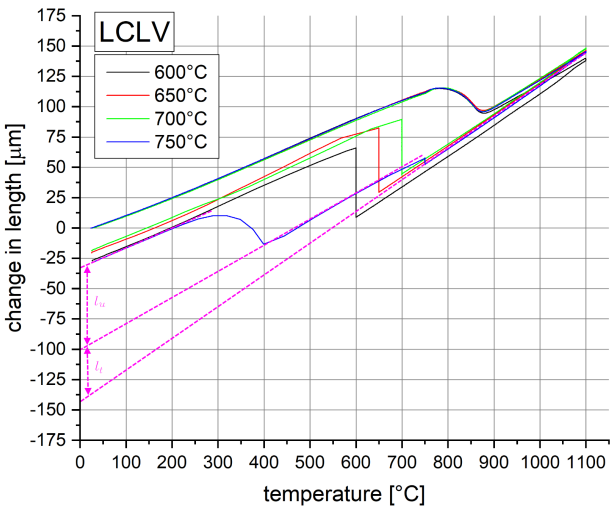

Fig. 3.5. Dilation-temperature plot for the LCLV alloy on all annealing temperatures.

Tab. 3.3.
Estimated and used fractions of transformed austenite during annealing period

	600°C (1hr)	650°C (1hr)	700°C (4, 16hr)	750°C (4hr)
BASE	1.0	1.0	0.8	0.45
LCLV	1.0	1.0	1.0	0.45
HCHV	1.0	1.0	1.0	0.65

It was found that calculating v_i in the manner described is highly sensitive to fluctuations in $X(t)$ which in itself is fluctuating on the raw input data ($\Delta L(t)$) delivered by the dilatometer. As such it was chosen to program the velocity estimation in Python. A Savitzky–Golay smoothening filter is used to slightly rub out noise in the data. This filter functions by fitting a moving local 4-th degree polynomial on the data points. This filter is added on the raw dilatometry data and the results of the fitting function. A piecewise cubic hermite interpolating polynomial (PCHIP) $\widehat{X}(t)$ is created from the $X(t)$ data points, to preserve monotonicity and reduce overshoot. This smooth continuous function can then trivially be differentiated to obtain $\widehat{X}(t)/\mathrm{dt}$. A schematic of the data flow to estimate the interface velocities is shown in **Fig. 3.6.**

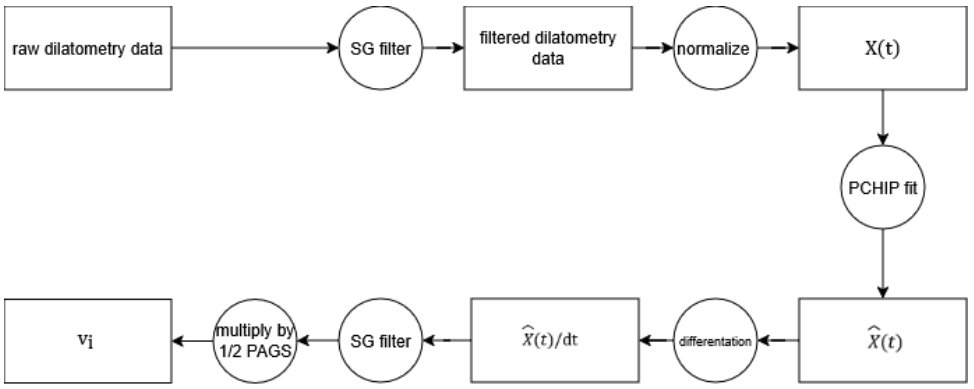

Fig. 3.6. Schematic overview of interface velocity estimation methodology.

3.2 Determination of the prior austenite grain size

The PAGS is required for the earlier described estimation of the interface velocity. Two methods were used to determine the grain size; (i) a chemical etching and an (ii) EBSD analysis were performed. All samples used in dilatometry and for the estimation of the interface velocity have been austenised for 5 minutes. To observe the effect of a longer austenisation duration, a sample austenised for 15 minutes was also quenched and prepared.

For method (i), all three alloys austenised for 5 minutes were analysed, and for 15 minutes austenisation only alloy HCHV. For method (ii) only alloy HCHV was analysed, austenised for 5 and 15 minutes.

3.2.1 PAGS determination (i): Chemical etching

To reveal the PAGS using chemical etching can be tricky, especially for alloys with low carbon and sulphur contents, as these elements tend to segregate to grain boundaries and aid in the observation after reacting with the etchant. A variation of the etchant reported in [22], [23] was produced, which consists of saturated aqueous picric acid with a small addition of hydrochloric acid and a wetting agent. The composition of the created and used etchant is given in **Tab. 3.4.** The content of HCl was increased from 2 to 6 drops until satisfactory results were obtained. Samples were etched for 2 minutes, then backpolished with 1 µm paste for 20 seconds and then ultrasonically cleaned before being observed under an optical microscope, until satisfactory results were achieved or no improvements were observed. This cycle of etching, polishing, cleaning and observing was repeated three to seven times depending on sample type.

Tab. 3.4.
Composition of created and used etchant

chemical (compound)	amount
saturated aqueous picric acid $(O_2N)_3C_6H_2OH$	100 ml
sodium dodecyl sulfate $CH_3(CH_2)_{11}OSO_3Na$	1.05 g
hydrochloric acid HCl	2-6 drops

To estimate the grain size the linear intercept method was used. Lines with known pixel length are placed randomly on the image and converted to microns by the scale bar, and the times the lines intersect with grain boundaries are counted. First, the total length L_T is determined by adding the different line segments, this is then divided by total intersect count P. This leads to the mean intercept length $\bar{l}$, i.e.:

$$P = \sum_i P_i \tag{3.8}$$

$$L_T = \sum_i L_i \tag{3.9}$$

$$\bar{l} = \frac{L_T}{P} \tag{3.10}$$

This was done four times, using sets of randomly placed horizontal and vertical lines. A total of ca. 500 intersection points were counted for both alloys.

3.2.1 PAGS determination (ii): EBSD analysis

Crystal orientations of ferrite were measured through EBSD. The measurements were performed using a JEOL JSM-IT800SHL scanning electron microscope. Samples were sanded

and polished according to standard metallographic procedures, although emphasis has to be put on the importance of the final OPS (0.25 micron paste) polishing step.

4. Experimental results

In this chapter the results of the performed experiments will be presented.

4.1 Prior austenite grain sizes

4.1.1 PAGS determination (i): Chemical etching

Fig. 4.1. shows the optical micrographs for all 5 minute austenised alloys. In both the BASE and HCHV samples, PAGS boundaries can be observed. In the LCLV sample, the microstructure does not reveal any clear grain boundary structure. In addition, the microstructure appears to be more refined. There has not been found a clear relation between the chemical composition and the ease of PAGS observation. One would expect a better observability of the PAGS with an increase of carbon content, as is clearly the case when comparing LCLV and HCHV, but the BASE alloy, which has the same (low) carbon content (but no vanadium) as LCLV, showcases a clear PAGS structure, which contradicts the theory of carbon levels dictating the ease of observation. One can only assume that the addition of low levels of vanadium present in LCLV and not in BASE prevent the carbon from showing the PAGS. Or it could be the case that more and different samples would have to be made and analysed to get a better average and overall result.

a) BASE 5 min

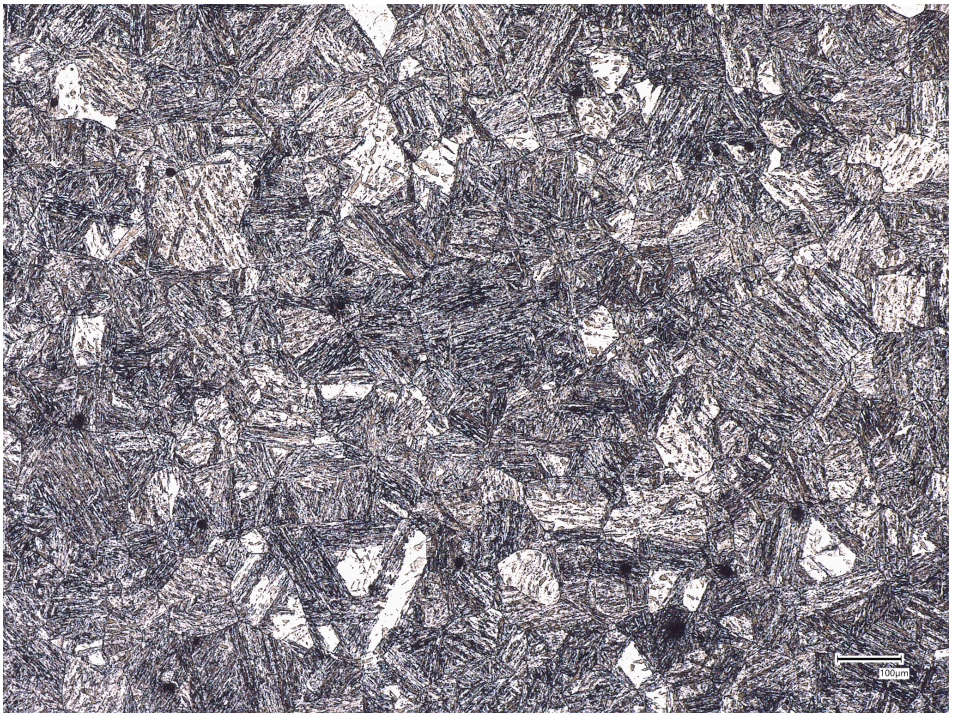

b) LCLV 5 min

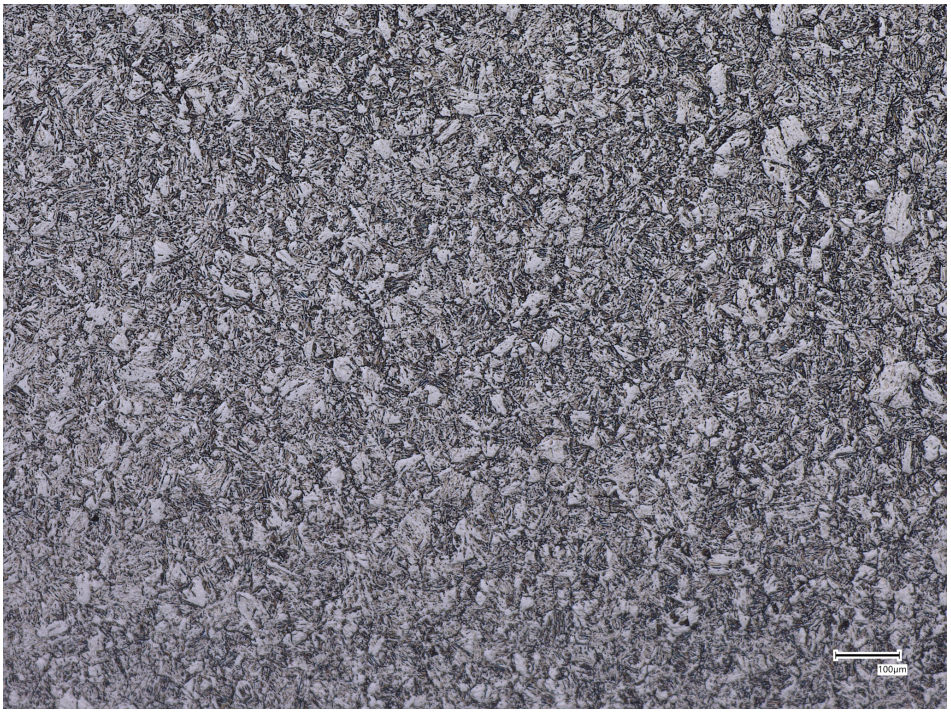

c) HCHV 5 min

Fig 4.1. Optical microstructures revealed with chemical etching for (a) BASE; (b) LCLV and; (c) HCHV alloys, austenised for 5 minutes at 1100 °C and subsequently quenched.

In the HCHV sample austenised for 15 minutes no clear prior austenite grain boundaries were observed, as seen in **Fig. 4.2**. The martensitic microstructure dominates the image, and prior grain size is expected to be larger with less boundaries visible at the magnification which was required for visibility in the 5 minute samples.

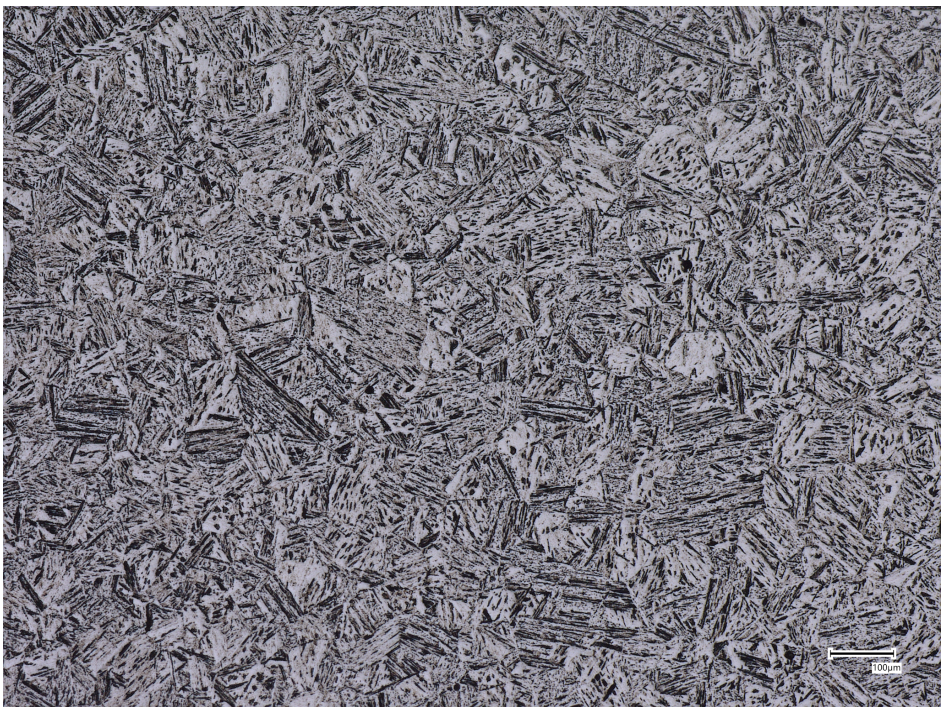

Fig. 4.2. Optical microstructure revealed with chemical etching for HCHV alloy, austenised for 15 minutes at 1100 °C and quenched.

For both the BASE and HCHV alloys the PAGS was analysed, for as mentioned earlier no PAGS boundaries were observable for the LCLV alloy. Prior austenite grain boundaries were selected from the image manually. One looks for the dark lines which disregard the other microstructural features. Even with decent etching results, differentiating the prior boundaries from the quenched martensitic structure can be challenging. Only boundaries with reasonable certainty have been selected. Note that this process is done by hand and can and will differ between individuals, i.e. it is in this case not a very scientific method. Nonetheless, if the data is not perfectly quantitatively reliable, it can give at least a ball park figure and give qualitative impressions. **Fig. 4.3.** shows the inferred prior austenite grain boundaries for the BASE and HCHV alloys (which are the analysed micrographs given in **Fig. 4.1.**).

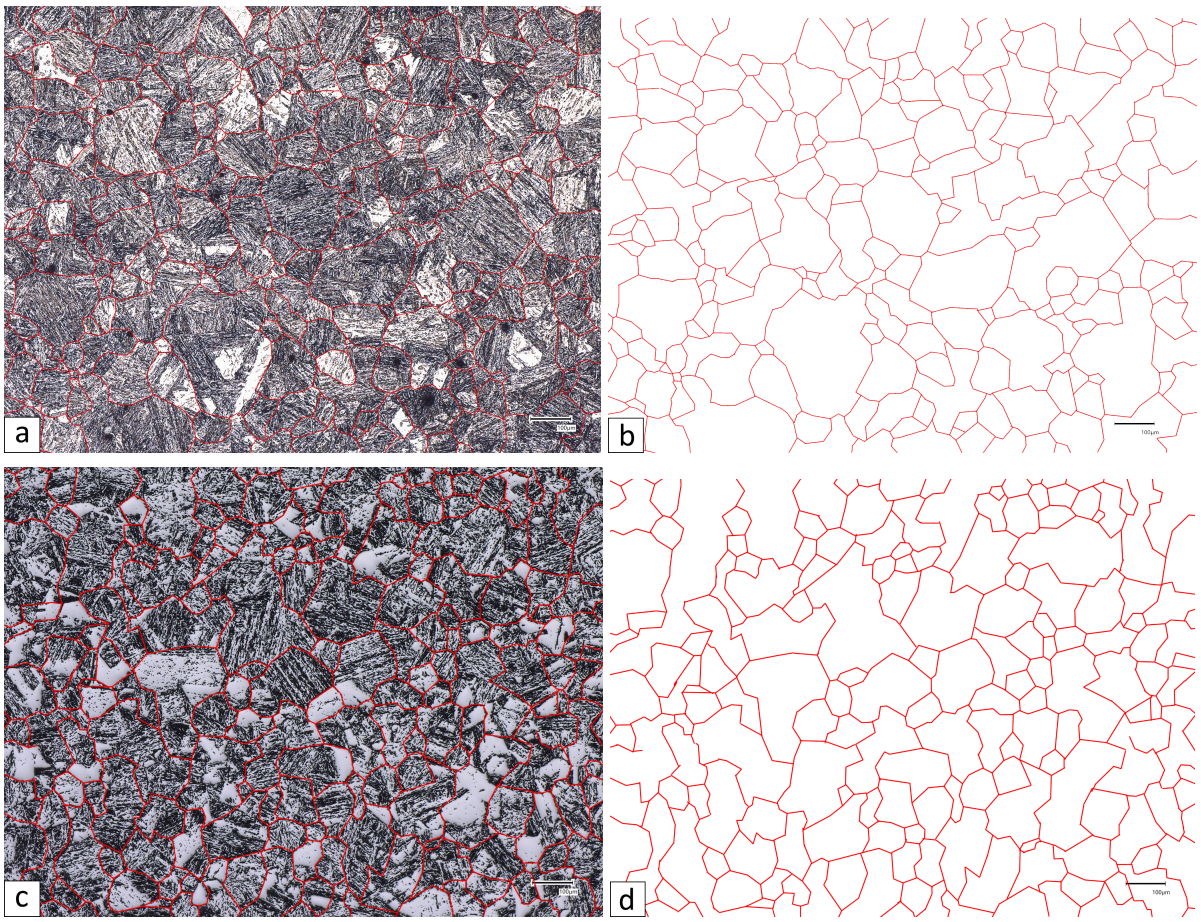

Fig. 4.3. Inferred prior austenite grain boundaries for: (a) BASE and; (c) HCHV alloys and isolated prior austenite grain boundaries for: (b) BASE and; (d) HCHV alloys.

Using the methodology discussed earlier, a mean intercept length of 82.8±2 μm was determined for the BASE alloy. For the HCHV alloy, a mean intercept length of 82.6±2 μm was found. This relates to an approximate equiaxed PAGS of the same value for both alloys.

4.1.2 PAGS determination (ii): EBSD analysis

A micrograph of the as-scanned HCHV sample austenised for 5 minutes is shown in **Fig. 4.4.** A clear martensitic microstructure is observed.

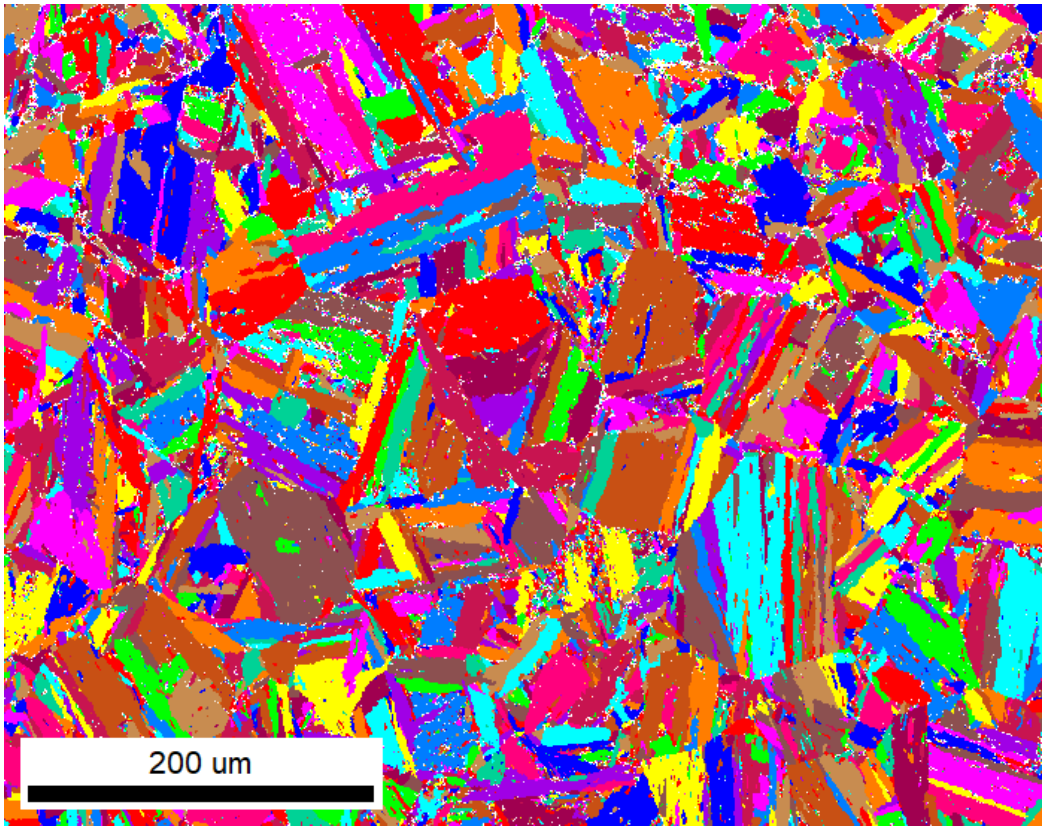

Fig. 4.4. Electron backscatter diffraction image of HCHV alloy austenised for 5 minutes.

To obtain an image of the prior austenite grain boundaries, a parent phase reconstruction needs to be performed. During the phase transformation the original microstructure may transform into several different crystallographic variants. The relationship between the parent (γ) grain orientation and the child (α) variants is known as the orientation relationship. If the Nishiyama-Wasserman orientation relationship is assumed, a prior austenite grain can transform into one out of twelve child variants. OIM-analysis software is used for parent phase reconstruction, using the NW-OR. The software calculates which variant out of the twelve is most likely to occur. The reconstructed microstructure is shown in **Fig. 4.5.**

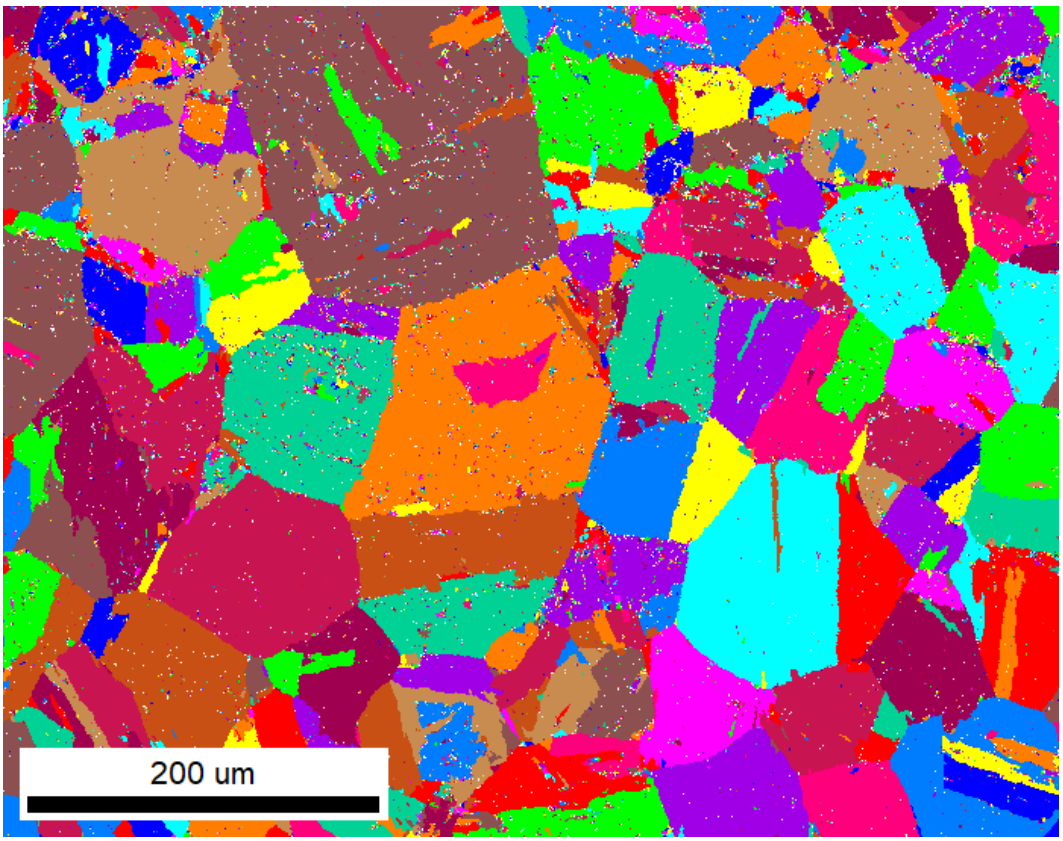

Fig. 4.5. Reconstructed parent austenite of HCHV 5 min using Nishiyama-Wasserman orientation relationship.

A statistical analysis is also performed. A minimum grain size of 7 pixels was chosen as a cut-off to exclude noise and thus prevent tons of miniscule grains occurring in the dataset. **Fig. 4.6.** showcases the grain size distribution of the reconstructed parent phase.

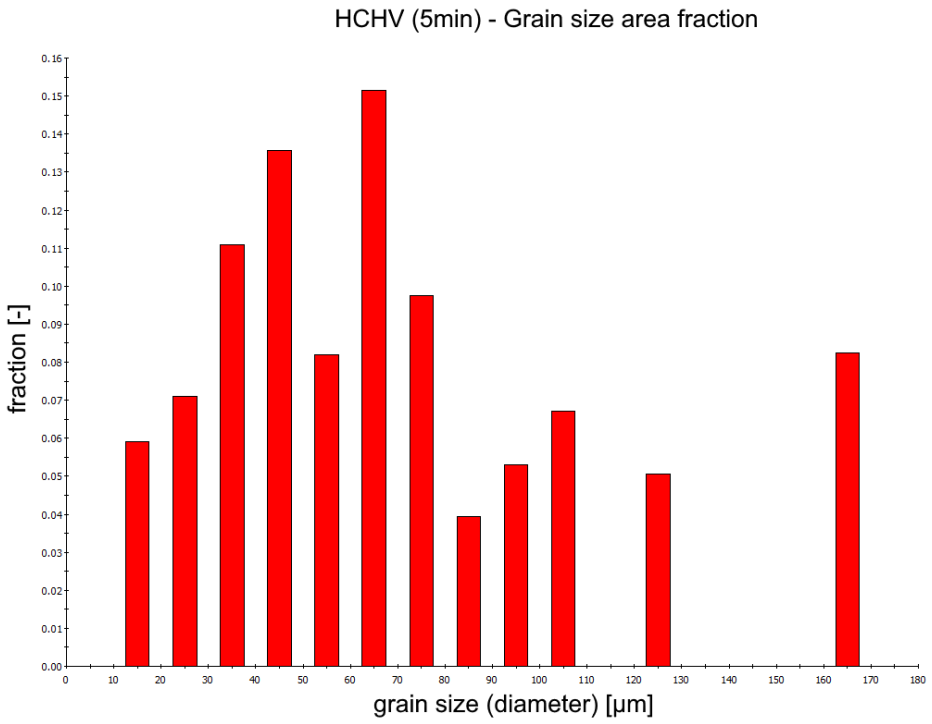

Fig. 4.6. With the grain size area fraction binned per grain size diameter for the HCHV alloy austenised for 5 minutes.

The area average $\overline{d_A}$ grain size is calculated as follows:

(3.11) $\overline{d_A} = \sum f_{A,i}\, d_i = 74\ \mu m$

It can be observed that the determined area-average grain size of 74 µm is close to the value of 83 µm found through chemical etching and the linear intercept method.

4.1.2 Effect of longer austenisation on PAGS

A similar analysis was performed on a HCHV sample which soaked for 15 minutes before quenching. The as-scanned micrograph is shown in **Fig. 4.7.** On first sight does the martensitic microstructure look very similar to the one found at shorter austenisation duration. The needles are slightly larger. The reconstructed phase image shown in **Fig. 4.8.** shows a great increase in grain size compared to the latter. In fact, it can be argued that the level of magnification is too high in order to properly quantify the PAGS. Nonetheless, qualitatively it can be concluded that a great increase in PAGS is achieved in an increase of soaking time of 200%, as one would expect.

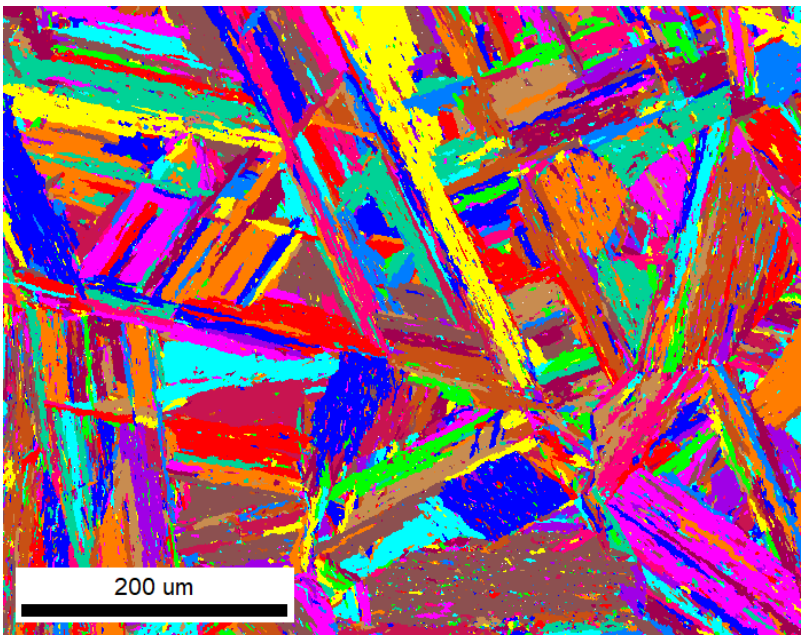

Fig. 4.7. Electron backscatter diffraction image of HCHV alloy austenised for 15 minutes.

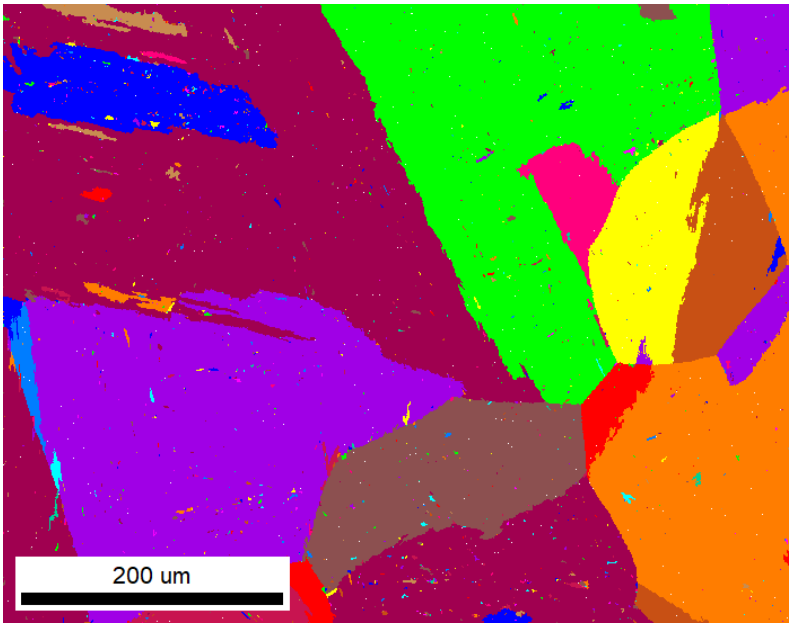

Fig. 4.8. Reconstructed parent austenite of HCHV 15 min using Nishiyama-Wasserman orientation relationship.

A similar statistical analysis is performed and a value of $\overline{d_A} = 173\ \mu m$ was found, although it must be reiterated that due to the same level of magnification of the scan a skewed image of grain sizes is observed. **Tab. 4.1.** summarises the found values for the prior austenite grain sizes.

Tab. 4.1.
Results PAGS determination method (i) and (ii)

Sample	method	characterisation	PAGS
BASE 5min	(i) chem. etching	linear intercept $\bar{l}$	82.8±2 µm
HCHV 5min	(i) chem. etching	linear intercept $\bar{l}$	82.6±2 µm
HCHV 5min	(ii) EBSD	area fraction $\overline{d_A}$	74±0.5 µm
HCHV 15min	(ii) EBSD	area fraction $\overline{d_A}$	173±0.5 µm

4.2 Dilatometry curve

An example of a section of raw plotted dilatometry data is showcased in **Fig. 4.9.** Here the first 30 minutes of the data for the LCLV sample austenised at 700°C is visible. Although this data and resulting plots are qualitatively useful, the data needs to be further processed in order to be used for the interface velocity estimation. It can also be observed that the phase transformation does not start during the cooling stage, and this is similarly found with the other alloys at different temperatures.

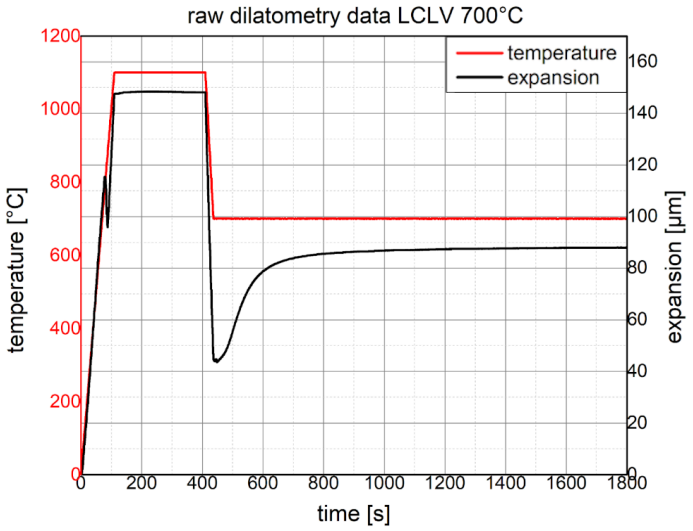

Fig. 4.9. First 30 minutes of raw dilatometry data showcasing temperature and change in length for LCLV alloy austenised at 700°C.

4.3 Interface velocity estimations

The earlier described methodology of obtaining the interface velocity has been applied to all treated steels. A half PAGS size r_γ of 30 µm was used, as previous literature indicated [21]. It is estimated to be similar enough to the own found values of ca. 37-42 µm. It has to be noted however, that for the LCLV alloys, the selected austenisation temperature of 1100°C is ca. 100

degrees higher than the calculated VC precipitate dissolution temperature of 994°C in a similar alloy [21]. This higher austenisation temperature might underestimate the grain sizes for the LCLV alloys, even if own analysis has shown that the BASE and HCHV alloys have similar PAGS. In either case, for this reason velocities have also been estimated for a half PAGS of 50 μm to obtain an experimental velocity range. The reason for choosing the higher end of the austenisation temperatures was to make sure a proper austenisation took place.

Although great care was taken with data selection and consequent calculations, it was found that, especially at the high temperatures of 700°C and 750°C the dilatometer gave artifacts and non-monotonic behaviour of the expansion at the onset of annealing. An example of this is showcased in **Fig. 4.10**. At, what has been chosen to be the onset of annealing indicated by the red line, two consecutive rises and falls of the measured expansion is found. For the methodology of determining the transformed fraction, this non-monotic behaviour can lead to undesired results (such as ferrite transforming back into austenite).

One could choose to select the moment of the actual start of annealing after these "artifacts", indicated by the green line. However, 57 seconds have passed (Δt between red and green line) of the sample being held at 750°C. Cutting away this minute just to get smooth results does introduce some questions about validity, especially since these first seconds are expected to be most important. On the other hand, the transformation is so sluggish and the maximum interface velocity is so low, that it could possibly not matter that much. It has been chosen whenever presented with such an artifact to select the onset of annealing at the respective red line, and to include these bumps.

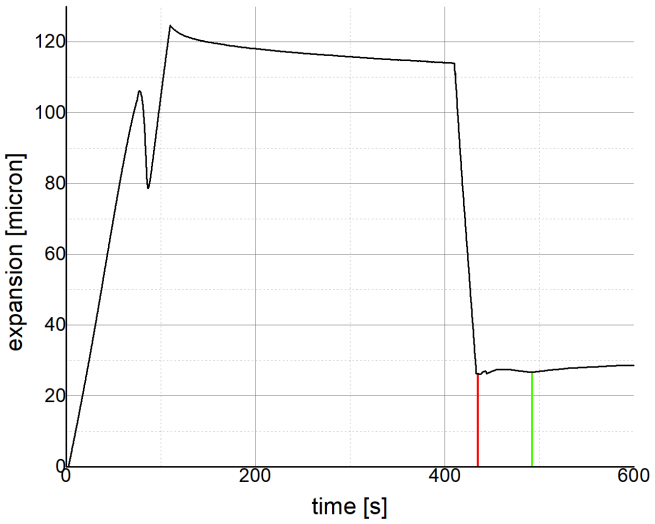

Fig. 4.10. Dilatometry curve of the first 10 minutes of thermal cycle of HCHV 750°C, indicating the non-monotonic artifact of the thermal expansion between red and green lines.

4.3.1 Effect of temperature on the transformation kinetics in the different alloys

BASE Alloy

Fig. 4.11. showcases the transformed fraction X(t) and the calculated interface velocities for the BASE alloy at each transformation temperature. One can observe the very rapid transformation of the alloy at 600°C, where a peak interface velocity is ca. 1300 nm/s. Note, that as mentioned earlier, the methodology used to calculate the interface velocity is more applicable to a planar

polygonal structure, where no large effects of grain curvature are taken into account. Potentially, at the temperatures of 600°C bainite can form, in which the bainitic ferrite would have more complex interactions with the kinetics where the relatively simple estimation used presently might not be applicable. Empirical equations for the bainite starting temperature B_S have indicated indeed that around 600°C, for some of the used alloys bainite could form, which will be presented later. According to the extension data for the BASE alloy at 750°C, the sample started to shrink continuously after initial transformation was completed until the measurement was stopped. Hence, the data for BASE 750°C after ca. 1000 seconds with respect to transformed fraction is potentially unreliable, since it isn't known what caused the sample to shrink. The initial peak in 750°C is due to the earlier described bump in the extension data, and is unknown if this is caused by an artifact due to dilatometry or an actual effect of extension due to phase transformation.

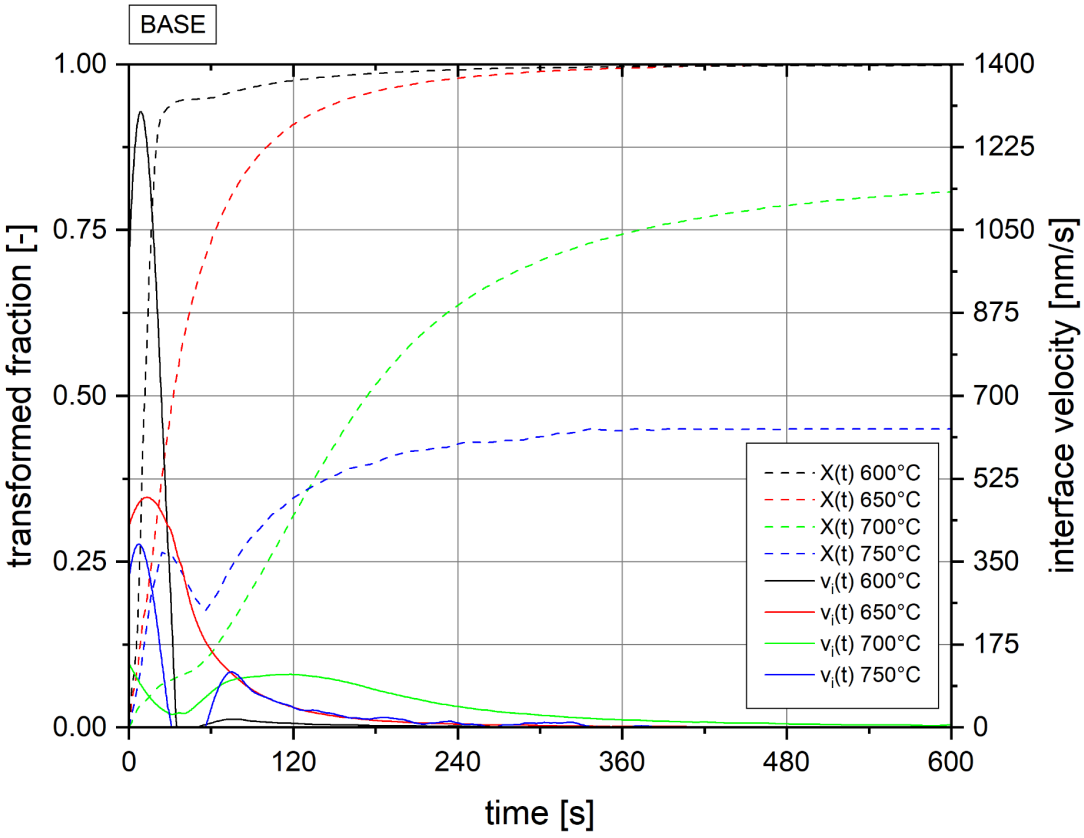

Fig. 4.11. Transformed fraction and interface velocity curves of the BASE alloy at all analysed temperatures.

LCLV Alloy

Fig. 4.12. showcases the transformed fraction X(t) and the calculated interface velocities for the LCLV alloy at each transformation temperature. For the LCLV alloy, it can be seen that the sample annealed at 650°C now transforms most rapidly, at a peak of ca. 350 nm/s. This is then followed by 700°C and 600°C annealing temperatures. At this lowest temperature the transformation is remarkably slower than for the BASE alloy. Qualitatively it has been found that the LCLV has a slightly lower bainite starting temperature, which might be of influence. All interface velocities

(peaks) lie lower compared to BASE, with the exception of 600°C. The same initial peak for 750°C can be observed, where again the same conclusions hold true.

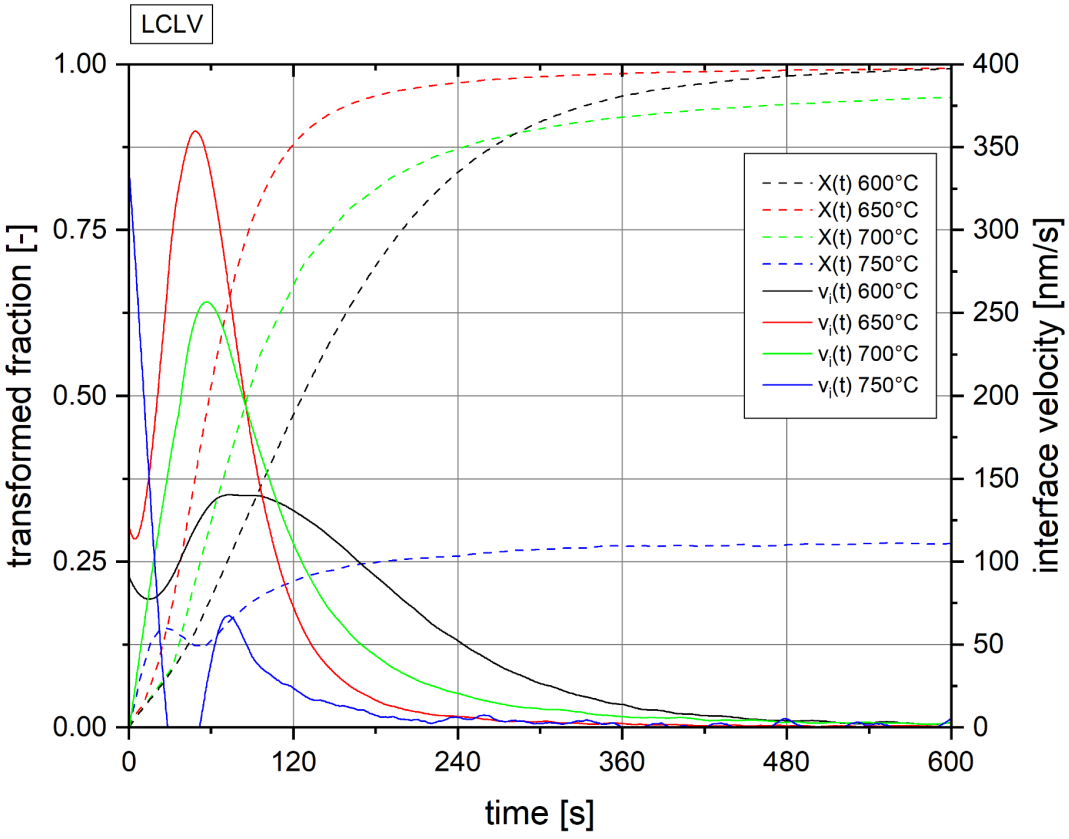

Fig. 4.12. Transformed fraction and interface velocity curves of the LCLV alloy at all analysed temperatures.

HCHV alloy

Fig. 4.13. showcases the transformed fraction X(t) and the calculated interface velocities for the HCHV alloy at each transformation temperature. It can be seen that in the initial stages the sample transformed most rapidly at 600°C, with a peak interface velocity of ca. 700 nm/s. Here it is followed by 650 and 700°C, which transform very similarly. After around 2 minutes of annealing, the 600°C annealing sample slows down in transformation rate, and tends to go to a plateau. It was estimated that the 1 hour of annealing was not enough for full transformation, and was estimated to with 15% austenite remaining (recall **Tab. 3.3.**).

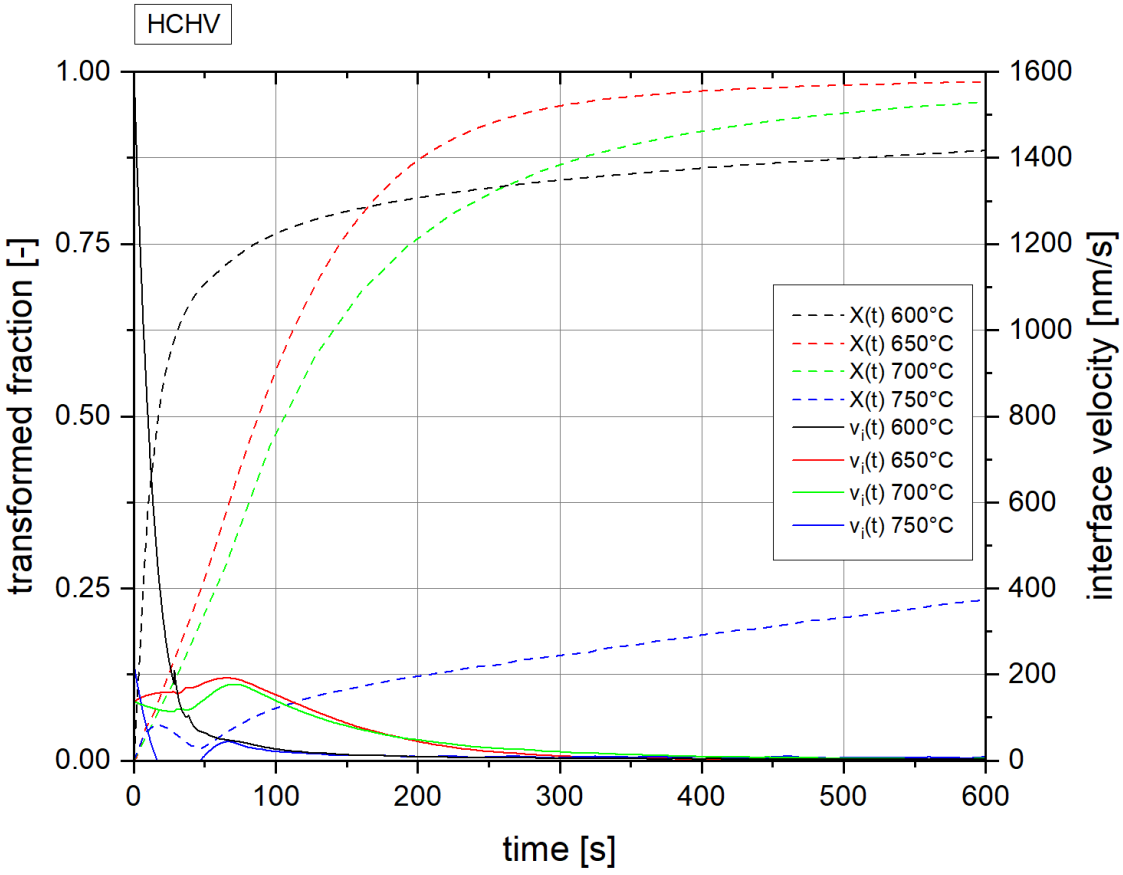

Fig. 4.13. Transformed fraction and interface velocity curves of the HCHV alloy at all analysed temperatures.

4.3.4 Effect of the carbon and vanadium content on the transformation kinetics at different temperatures

In addition, it can be useful to view the transformation curves per analysed temperature. **Fig. 4.14.** shows the calculated transformed fraction per selected velocity for the three alloys.

At the intermediate temperature of 650°C, the high vanadium content of HCHV leads to the slowest transformation. This could be understood in the traditional theory of most levels of segregation and precipitation behaviour affecting the transformation in this steel at this temperature due to the highest alloying content. The precipitation (of presumably VC) and the segregation of vanadium to the grain boundaries has a retarding effect larger than in LCLV at this temperature. In addition, it was found in previous literature that the content of manganese in the precipitates increases slightly with decrease in temperature for the LCLV, leading to more manganese consumption and less energy dissipation of said element and thus a faster phase transformation [24]. These changes were small however, and only given when decreasing the temperature from 700 to 650°C. The higher carbon content can additionally stabilize the austenite to a greater degree. However, some doubts due to modelling and experimental results on this theory are presented now.

It can be observed that for 600°C, a low amount of V and C (in the LCLV alloy) leads to a great retardation of the phase transformation (with respect to BASE and more importantly

HCHV alloys). Normally, one would expect that with increasing alloying content, especially with regards to substitutional elements, an increase of segregation and related solute drag and energy dissipation would occur and affect the transformation kinetics, as just concluded for 650°C. In the case of vanadium, however, this is less the case as is found in modelling results to be presented and discussed later. In the modeling it was found that the magnitude of energy dissipation due to vanadium segregation is minute relative to the total energy dissipation and as such the transformation kinetics of the alloys have to be understood in terms of precipitation behaviour of vanadium (and interacting carbon), since the manganese levels and related energy dissipation are constant in the alloys.

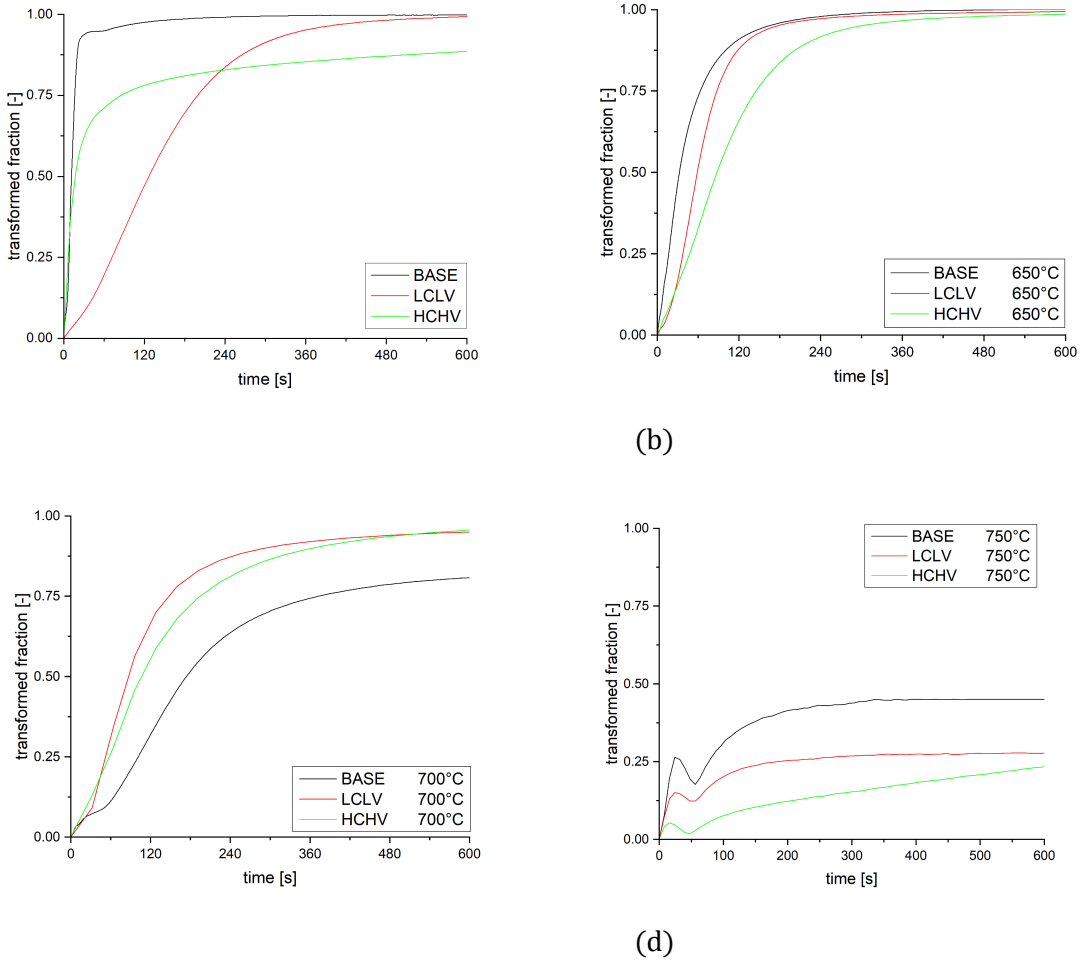

Fig. 4.14. Transformed fraction of the three alloys for all temperatures: (a) 600°C; (b) 650°C; (c) 700°C and; (d) 750°C.

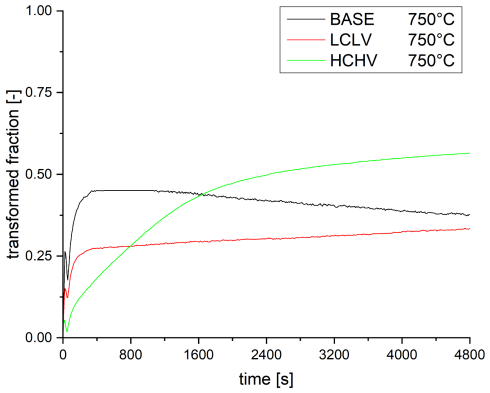

Fig. 4.15. Transformed fraction 750°C shown over a longer timescale.

One could presume that a difference in driving force for transformation between LCLV and HCHV would exist due to different alloying contents, which would beat the retarding effects of segregation and precipitation (which are noticeable at the other temperatures) at the temperature of 600°C, where at these lower temperatures it might be of less influence since diffusivity of the elements is lower. However, found chemical driving forces for transformation of previous similar alloys indicated that only minute differences exist between LCLV and HCHV alloys; a change ΔG_{Chem} of only 2 J/mol was found at 700°C (and no difference for 650°C)[25]. Presumably, the stoichiometric increase of carbon and vanadium as austenite and ferrite stabilisers respectively compensated one another, leading to no increase of chemical driving force for transformation with increase in alloying.

A factor which is different, however, is the driving force $\Delta G_{V,p}$ for carbide precipitation in ferrite, which was found to increase with decrease of annealing temperature and increase of vanadium content [24]. Hence, it could be postulated that an increase of precipitation of VC occurs at 600°C HCHV compared to LCLV 650°C. And since it was also found that energy dissipation due to Zener pinning effects on grain boundary movement is very low (compared to the other dissipation) it could be the case that the extra consumption of carbon due to VC precipitation in the HCHV alloy at 600°C promotes its phase transformation kinetics compared to the LCLV alloy. Still this theory is not fully concrete, since the BASE alloy at 600°C transforms even faster than the HCHV alloy, and in that alloy there are no precipitates to be formed to consume carbon, which means that the difference of kinetics between HCHV and LCLV at 600°C must be related to unconsumed vanadium in the LCLV alloy which slows the interface, yet modeling results indicate that the energy dissipation of vanadium is very low.

Additionally, this theory about an increase of V and C content actually increasing the transformation kinetics (and not decreasing) should also be the case for the different temperatures, but as is presented at 650°C and seen at 700°C, the HCHV transforms slower than LCLV.

Thus, perhaps a different reason for VC precipitation has to be considered. As was discussed earlier, a possible formation of bainite at 600°C could occur, which would influence the phase transformation kinetics. However, even a bainitic influence theory must support why the BASE alloys transform fast, but the LCLV alloy transforms slow. Four different empirical equations, which all include C, V and Mn were used to determine the bainite start temperature for the used alloys, shown in **Tab. 4.2**, full formulas are given in **Appendix A1**. It can be seen, with

exception of the first row (which equation is for forged steels but included for cross checking), that all alloys lay in a critical bainite starting regime of around 600°C. However, no great differences exist between LCLV and BASE, they are of the order of 10-30°C, which is often lower than the accuracy of these empirical equations.

In all temperatures except at 700°C the BASE alloy transforms the most rapidly, as can be expected since there is no vanadium to influence the dynamics by manner of segregation and precipitation. It is not known why, at the temperature of 700°C the exception exists and the alloy without vanadium transforms the slowest. Do note however, that all dilatometer experiments have been performed once, and that perhaps a repetition of the experiments would shed more light on noteworthy exceptions. In addition, a slight bump and decrease in slope can be seen for the BASE transformed fraction at this temperature. If this is an artifact due to dilatometry (and thus could be ignored) one can imagine the base curved shifted horizontally to the left until the slopes of the curves align at around X(0) to X(0.2). This was done, but even then the BASE alloy would transform the fastest after around X(0.25).

At 750°C, the results of the transformed fraction of BASE after ca. 1000s are best excluded, since there are doubts about the validity of the dilatometer data, shown in **Fig. 4.15**. It can be seen however, that HCHV initially transforms slower, but continues to transform while LCLV reaches a plateau and only transforms very slowly afterwards.

Tab. 4.2. Calculated bainite start temperatures B_S.

BASE [°C]	LCLV [°C]	HCHV [°C]	Ref.
610.9	584.5	539.1	[26]
631.2	619.9	590.3	[27]
558.7	547.8	534.7	[28]

4.3.5 Significance of sample orientation

As presented earlier, the possibility of anisotropy affecting the dilatometry results was analysed. From **Fig. 4.16.** it can be inferred that possible banding in the microstructure would occur on and parallel to the r_d - t_d plane. This is showcased in figure X, where it is mentioned again that the samples' thermal expansion is measured along its length, so along the direction of the sample name.

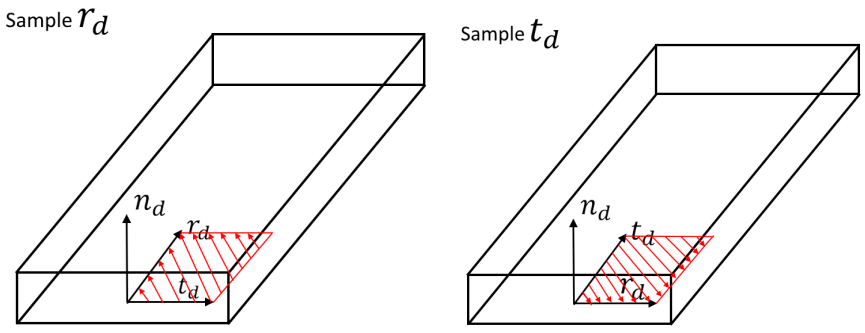

Fig. 4.16. Orientation of possible banding anisotropy in specimens indicated in original steel slab coordinate

As can be observed, the possible banding surfaces are in both samples parallel to the flat surface side of the samples, i.e. parallel to the r_d - t_d plane. Red arrows from the transverse direction towards the rolling directions have been drawn, which is the only possible consistent repeating difference between sample types. **Fig. 4.17.** showcases the change in length of the HCHV r_d and t_d samples transformed under 600°C and 650°C.

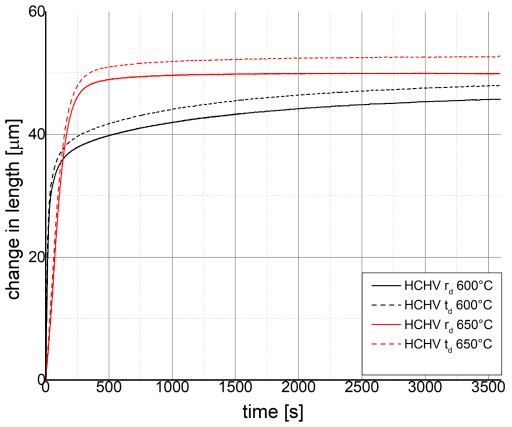

Fig. 4.17. Change in length in the annealing section of the HCHV r_d and t_d samples annealed at 600°C and 650°C.

It can be observed that the change in length in the early stages of annealing are very minimal, and would thus result in very similar initial transformation kinetics. It can be also seen that the t_d samples have a higher plateau of total expansion. At the later stages of the determination of transformed fraction and resulting interface velocity the differences would have a larger effect, since the r_d samples reach full transformation slightly faster.

It is not known if many preliminary conclusions can be made from just four dilatometry curves, but it could be concluded that the t_d samples are a bit slower in reaching full transformation. It is not known if this is related to the direction of the red drawn arrows in **Fig. 4.16.** with respect to the length of the sample, i.e. the dilatometer measuring axis.

4.3.6 Interface velocity maxima

To obtain a range of interface velocities both a half PAGS of 30 and 50 micron was used in the calculation of the interface velocity. This can be seen in **Fig. 4.18.** where these plots are shown for the LCLV alloy. Per temperature a peak velocity range can then be obtained. The peak velocities are given in **Tab. 4.3.** Logically, it can be observed that the interface velocities are higher for the calculations with $r_\gamma = 50\ \mu m$, since this is essentially a scaling factor.

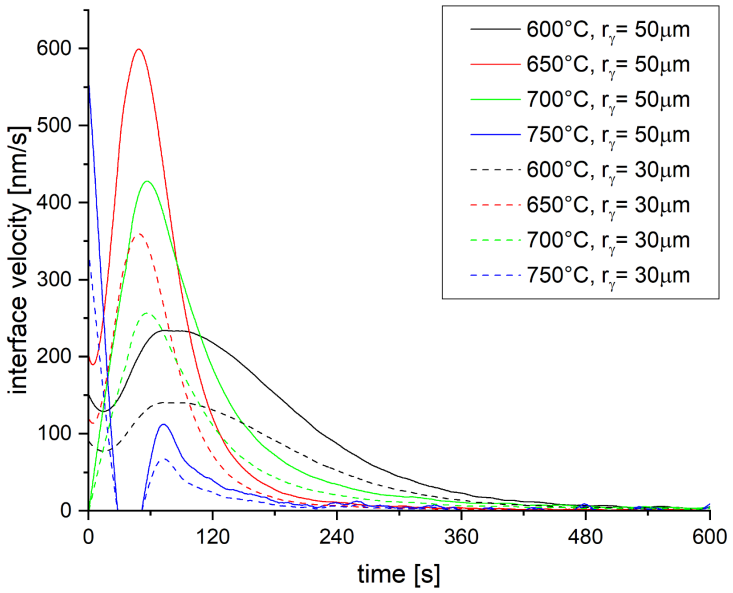

Fig. 4.18. Interface velocities of LCLV alloys with half PAGS of 30 and 50 µm used in calculations.

For the temperature of 750°C, the second peak is chosen as the actual peak velocity, and thus not the rapid initial transformation.

Tab. 4.3. Obtained peak interface velocities for LCLV

Temperature	$r_\gamma = 30$ µm	$r_\gamma = 50$ µm
600	140 nm/s	232 nm/s
650	359 nm/s	599 nm/s
700	257 nm/s	427 nm/s
750	67 nm/s	112 nm/s

5. Energy dissipation model

5.1 General description

To better understand the conditions at the migrating α/γ interface, which can induce the precipitation of carbides, the kinetics of the phase transformation are modeled. As mentioned earlier, during the phase transformation solutes may segregate at the moving interface. As Hillert and Sundman suggested, this solute-drag contributes to the dissipation of the Gibbs free energy of the system, in addition to the occurring partition and redistribution of the solutes into the bulk and the crystal lattice change from FCC to BCC.

A similar approach has been used which was proposed by Miyamoto et al. for a ternary alloy [29]. Extensions have been made to this approach to apply it to the quaternary alloys analysed presently. Chemical potentials of Fe and the solutes C, V and Mn within the α/γ interface region are defined according to the Hillert-Staffonson sub-lattice model. [30] [31] The regular solution model is used to describe the thermodynamics of the quaternary Fe-C-Mn-V system assuming random mixing of the components each occupying a specific sublattice . This approach considers both ferrite and austenite phases composed of two sublattices. One (referred to as sublattice 1) is occupied by the solvent (Fe) and all the substitutional elements in the alloy. The other sublattice (called sublattice 2) is partially occupied by the interstitially dissolved element. The vacant sites in sublattice 2 are treated as an additional component, the vacancy Va. The interstitial and substitutional solution can then be modelled as a stoichiometric phase with the vacancy as a component, that is; $(Fe, Mn, V)_a$ and $(C, Va)_c$. The following relations exist between the site fractions y_i and mole fraction x_i:

$$y_{Fe} = 1 - y_{Mn} - y_V \; ; \; y_{Mn} = \frac{x_{Mn}}{1-x_C}; y_V = \frac{x_V}{1-x_C}; y_C = \frac{x_c}{1-x_C} \tag{5.1}$$

The chemical potentials are approximated as follows:

$$\mu_C = G_C^0 + RT\varepsilon_{MnC}y_{Mn} + RT\varepsilon_{VC}y_V + RT\, ln\frac{y_C}{1-y_C} + E_C(X) \tag{5.2}$$

$$\mu_V = G_V^0 + RT\varepsilon_{VC}y_C + RT\, ln\,\frac{y_V}{y_{Fe}} + E_V(X) \tag{5.3}$$

$$\mu_{Mn} = G_{Mn}^0 + RT\varepsilon_{MnC}y_C + RT\, ln\,\frac{y_{Mn}}{y_{Fe}} + E_{Mn}(X) \tag{5.4}$$

Where y_i is the concentration of element i in the interface. The dependence of X on the concentration is omitted.

A triangular potential well is used to describe the chemical potentials of the solutes in the ferrite-austenite interface region, shown in **Fig. 5.1**.

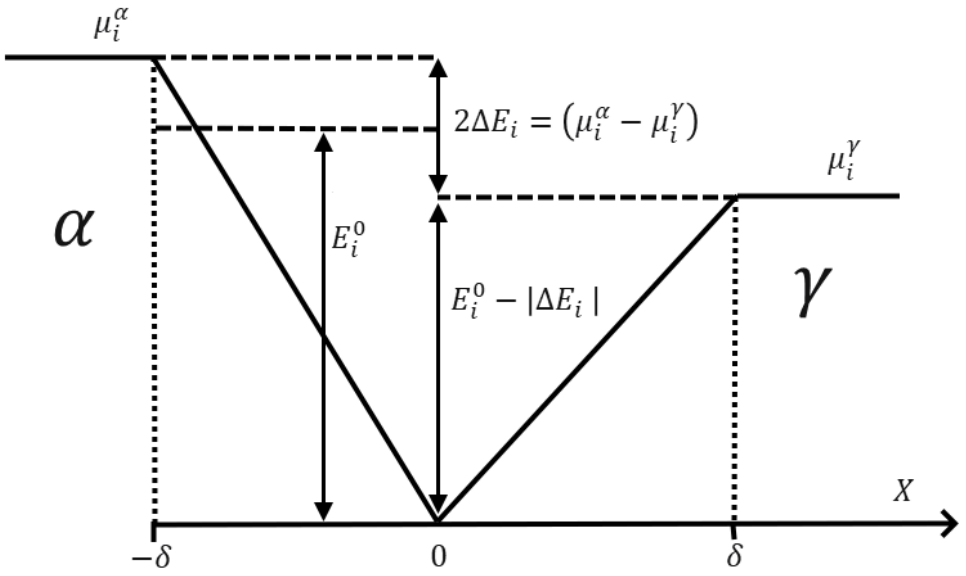

Fig. 5.1. Schematic diagram of chemical potential of solute *i* in the α/γ interface region.

The diffusion fluxes of the substitutionals are given by [16]:

(5.5) $$J_V = -\frac{D_V}{RTV_m} y_{Fe} y_V \frac{d}{dX} \mu_V$$

(5.6) $$J_{Mn} = -\frac{D_{Mn}}{RTV_m} y_{Fe} y_{Mn} \frac{d}{dX} \mu_{Mn}$$

Where D_V and D_{Mn} are the trans-interface diffusivities of the substitutional solutes and V_m the molar volume.

The interaction energy of the solute with the interface is given as:

(5.7) $$E_i(X) = -(\Delta E_i + E_i^0) - \frac{E_i^0 + \Delta E_i}{\delta} X, \qquad -\delta < X < 0$$

(5.8) $$E_i(X) = -(\Delta E_i + E_i^0) + \frac{E_i^0 - \Delta E_i}{\delta} X, \qquad 0 < X < \delta$$

Where ΔE_i is half the difference in the free energy of element *i* between α and γ and E_i^0 is the binding energy between element *i* and the interface. Due to the differences in diffusivity of carbon and the substitutional elements it is assumed that in the early stages of transformation Mn and V do not partition between bulk and γ, and thus α grows in PE conditions. For this reason, the elemental site fractions y_i^0 at $X = -\delta$, which are the initial conditions of the system of CDE, are set equal to the site fractions in α formed in PE conditions.

Within the diffuse interface the concentration profile must obey Fick's second law:

(5.9) $$\frac{\partial}{\partial t} y_i = -V_m \frac{\partial}{\partial X} J_i$$

Under steady state condition, the partial derivative of the concentration profile is equal but opposite to the interface velocity times the partial derivative with respect to distance coordinate of the concentration profile:

(5.10) $\frac{\partial}{\partial t}y_i = -\,v\frac{\partial}{\partial X}y_i$

Combining these equations leads to the following balance equation to be fulfilled:

(5.11) $\frac{\partial}{\partial X}(vy_i - J_i V_m) = 0$

Substituting the equations for the chemical potentials into the diffusion flux equation, the following expressions are formed:

(5.12) $J_C = -\frac{D_C}{V_m}\left[\frac{\partial y_C}{\partial X} + \varepsilon_{MnC}\left(1 - y_c\right)y_c\frac{\partial y_{Mn}}{\partial X} + \varepsilon_{VC}\left(1 - y_c\right)y_c\frac{\partial y_V}{\partial X} + \frac{1}{RT}\frac{\partial E_C}{\partial X}\right]$

(5.13) $J_V = -\frac{D_V}{V_m}\left[\varepsilon_{VC}\left(1 - y_{Mn} - y_V\right)y_V\frac{\partial y_C}{\partial X} + \left(1 - y_{Mn}\right)\frac{\partial y_V}{\partial X} + y_V\frac{\partial y_{Mn}}{\partial X} + \frac{1}{RT}\frac{\partial E_V}{\partial X}\right]$

(5.14) $J_{Mn} = -\frac{D_{Mn}}{V_m}\left[\varepsilon_{MnC}\left(1 - y_{Mn} - y_V\right)y_{Mn}\frac{\partial y_C}{\partial X} + \left(1 - y_V\right)\frac{\partial y_{Mn}}{\partial X} + y_{Mn}\frac{\partial y_V}{\partial X} + \frac{1}{RT}\frac{\partial E_{Mn}}{\partial X}\right]$

By substituting these diffusional fluxes into the balance equation, the following system of coupled ordinary differential equations is obtained:
(5.15 to 5.17)

$$\frac{\partial y_C}{\partial X} + \varepsilon_{MnC}y_C\left(1 - y_c\right)\frac{\partial y_{Mn}}{\partial X} + \varepsilon_{VC}y_C\left(1 - y_C\right)\frac{\partial y_V}{\partial X} = -\frac{y_C\left(1-y_C\right)}{RT}\frac{\partial E_C}{\partial X} - \frac{v}{D_C}\left(y_C - y_C^0\right)$$

$$\varepsilon_{VC}y_V\left(1 - y_V - y_{Mn}\right)\frac{\partial y_C}{\partial X} + y_V\frac{\partial y_{Mn}}{\partial X} + \left(1 - y_{Mn}\right)\frac{\partial y_V}{\partial X} = -\frac{y_V\left(1-y_V-y_{Mn}\right)}{RT}\frac{\partial E_V}{\partial X} - \frac{v}{D_V}\left(y_V - y_V^0\right)$$

$$\varepsilon_{MnC}y_{Mn}\left(1 - y_V - y_{Mn}\right)\frac{\partial y_C}{\partial X} + y_{Mn}\frac{\partial y_V}{\partial X} + \left(1 - y_V\right)\frac{\partial y_{Mn}}{\partial X} = -\frac{y_{Mn}\left(1-y_V-y_{Mn}\right)}{RT}\frac{\partial E_{Mn}}{\partial X} - \frac{v}{D_{Mn}}\left(y_{Mn} - y_{Mn}^0\right)$$

With y_i^0 the concentration of the solutes in ferrite. The last term in the equation formulated from the carbon flux, namely $\frac{v}{D_C}\left(y_C - y_C^0\right)$ is neglected due to the much higher diffusivity of C with respects to the substitutional solutes. ε_{MnC} and ε_{VC} are the Wagner interaction parameters regulating the interaction of manganese-carbon and vanadium-carbon within the interface region. The interaction between manganese-vanadium is neglected, however due to the coupling of the system of equations through carbon, an interaction will still be visible. This system of equations can then be formulated in implicit matrix form:

(5.18) $M(x, y)\frac{dy}{dx} = r(x, y)$

Which leads to:

$$(5.19)\quad \begin{pmatrix} 1 & \varepsilon_{Mn} y_C (1-y_C) & \varepsilon_{VC} y_C (1-y_C) \\ \varepsilon_{MnC} y_{Mn} (1-y_V-y_{Mn}) & 1-y_V & y_{Mn} \\ \varepsilon_{VC} y_V (1-y_V-y_{Mn}) & y_V & 1-y_{Mn} \end{pmatrix} \begin{pmatrix} \frac{\partial y_C}{\partial X} \\ \frac{\partial y_{Mn}}{\partial X} \\ \frac{\partial y_V}{\partial X} \end{pmatrix} =$$

$$\begin{pmatrix} -\frac{y_C(1-y_C)}{RT} \frac{\partial}{\partial X} E_C \\ -\frac{y_{Mn}(1-y_V-y_{Mn})}{RT} \frac{\partial}{\partial X} E_{Mn} - \frac{v}{D_{Mn}^{trans}} (y_{Mn} - y_{Mn}^0) \\ -\frac{y_V(1-y_V-y_{Mn})}{RT} \frac{\partial}{\partial X} E_V - \frac{v}{D_V^{trans}} (y_V - y_V^0) \end{pmatrix}$$

To calculate the effect of solute drag on the α growth kinetics, the concentration profiles of carbon and the substitutional solutes at the interface are thus first calculated. Afterwards, the dissipation of the Gibbs free energy due to substitutional interface segregation is calculated using the equations from Hillert and Sundman [16]:

$$(5.20)\quad \Delta G_{SDE}^{V} = -\frac{V_m}{v} \int_{-\delta}^{\delta} J_V \frac{d}{dx} \Delta\mu_V dX$$

$$(5.21)\quad \Delta G_{SDE}^{Mn} = -\frac{V_m}{v} \int_{-\delta}^{\delta} J_{Mn} \frac{d}{dx} \Delta\mu_{Mn} dX$$

Where X is the coordinate of the diffuse interface between -δ and δ ,with its origin at the centre of interface with thickness 2δ. The energy dissipation ΔG_{SDE} is obtained by integration within the interface, and does not include energy dissipation due to a potential solute spike formed next to the interface.

The contribution of energy dissipation due to interface friction is represented by:

$$(5.22)\quad \Delta G_{MOB} = -\frac{v_i}{M}$$

Where M is the intrinsic mobility of the interface. For reconstructive phase transformations with incoherent interfaces, the intrinsic mobility is noted as a thermally activated following the Arrhenius relation:

$$(5.23)\quad M = M_0 e^{-Q/RT}$$

Where M_0 is the pre-exponential factor, Q the activation energy, R the gas constant and T the temperature. M_0 has been found to change widely in literature, which leads to widely changing values of the intrinsic mobility.

Elemental segregation of the substitutional solutes i were calculated with the following equation:

(5.24) $\Delta X_i = \frac{1}{V_a}\int_{-\delta}^{\delta}\left(y_i - y_i^0\right)dX$

Where $V_a = 0.0118$ nm^3/atom is the atomic volume.

6. Model results and discussion

The results of the presented model are shown in this chapter. Results will be focused on the LCLV alloy, unless stated otherwise, since model results between different alloys are quantitatively (and thus qualitatively too) very similar.

6.1 Overview

6.1.1. Model input parameters

Tab. 6.1. Shows the used input parameters of the model. The bold faced parameters (for 650°C and 700°C) were obtained through Thermocalc. For the temperatures of 600°C and 750°C the data was unable to be obtained through Thermocalc by the author and hence estimated. The Wagner parameters were estimated through linear extrapolation and the values for the diffusivity were approximated through exponential extrapolation, where an Arrhenius type of relation is assumed.

Tab. 6.1. Used Wagner interaction parameters and solute diffusivities.

Temp.	ε_{MnC}	ε_{VC}	$D^{\alpha}_{Mn}[nm^2/s]$	$D^{\alpha}_{V}[nm^2/s]$
600°C	-7.36	-26.94	0.32	0.172
650°C	**-6.79**	**-25.19**	**3.205**	**1.864**
700°C	**-6.22**	**-23.44**	**25.64**	**15.85**
750°C	-5.65	-21.69	167	109

Additionally, values for the pre-exponential factor, the activation energy and binding energies are used as given in **Tab. 6.2**, unless stated otherwise.

Tab. 6.2. Standardly used parameters

M_0 [m mol/s J]	Q [kJ/mol]	E^0_C [kJ/mol]	E^0_V [kJ/mol]	E^0_{Mn} [kJ/mol]
0.38 [32]	140	10 [19]	7.7 [33]	7 [33]

6.1.2. Model results

Fig. 6.1. encompasses the model results. It can be observed that the energy dissipation due to manganese is orders of magnitude greater than vanadium, due to the higher concentration of manganese in the steels.

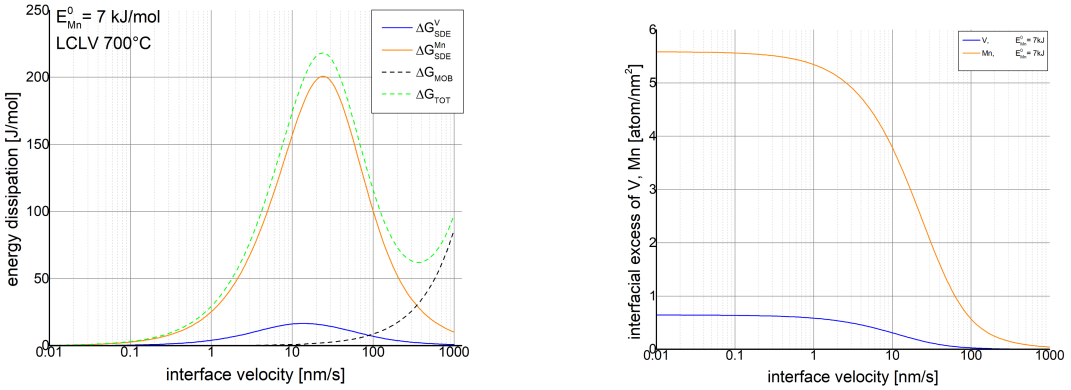

Fig. 6.1. (a). Energy dissipation and; (b) Elemental segregation of the substitutional solutes.

The total energy dissipation $\Delta G_{TOT} = \Delta G_{SDE}^{Mn} + \Delta G_{SDE}^{V} + \Delta G_{MOB}$ is through all interface velocities dominated by the dissipation due to manganese. At higher interface velocities, the energy dissipation due to interface friction dominates. The related elemental segregation of manganese is much higher than that of vanadium.

6.2 Concentration profiles

Results of the calculated concentration profiles of the LCLV 700°C are shown. Results are plotted per swept interface velocity. Clearly visible is the increased concentration throughout the interface with decreasing velocity. This naturally makes sense since more time is allowed for distribution of the solutes. Some instability might be visible at austenite side (δ=1) at the lowest swept interface velocity of 0.01 nm/s, indicated with the red arrow, where in the vanadium profile a spike can already be observed. This trend of instability at lower interface velocities is seen in more results and is discussed in **Appendix A2.**

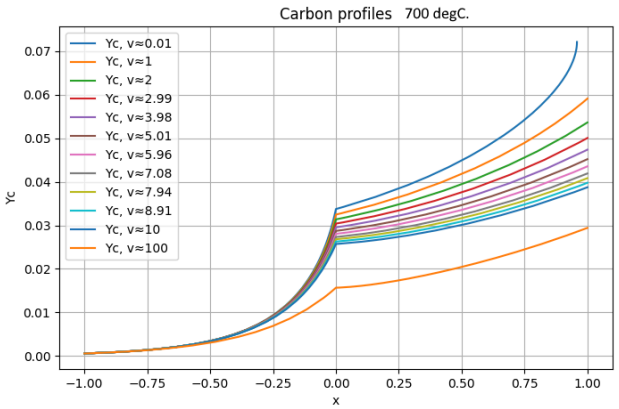

Fig. 6.2. Carbon profiles in the interface for LCLV 700°C for different values of the interface velocity in nm/s.

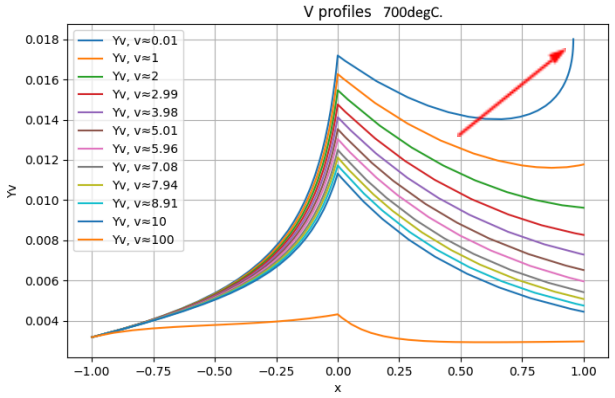

Fig. 6.3. Vanadium profiles in the interface for LCLV 700°C for different values of the interface velocity in nm/s.

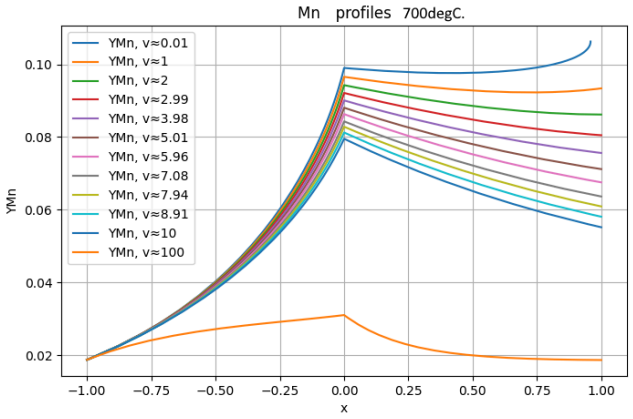

Fig. 6.4. Manganese profiles in the interface for LCLV 700°C for different values of the interface velocity in nm/s.

6.2 Effects of different parameters

6.2.1 Role of temperature

Fig. 6.5. and **Fig. 6.6.** plot the energy dissipation and segregation on all analysed temperatures. Multiple observations can be made. Firstly, large spikes and discontinuities of the calculated energy dissipation and elemental segregation around a lower interface velocity can be seen. These spikes are a result of numerical instability which is discussed in **Appendix A2.** As expected, a lowering of the energy dissipation with increase of annealing temperature can be observed. A peak shift towards higher interface velocities is due to an increase of diffusivity at higher temperatures. Segregation increases with temperature but has a maximum at 700°C, where it can be seen to be substantially higher than at 750°C.

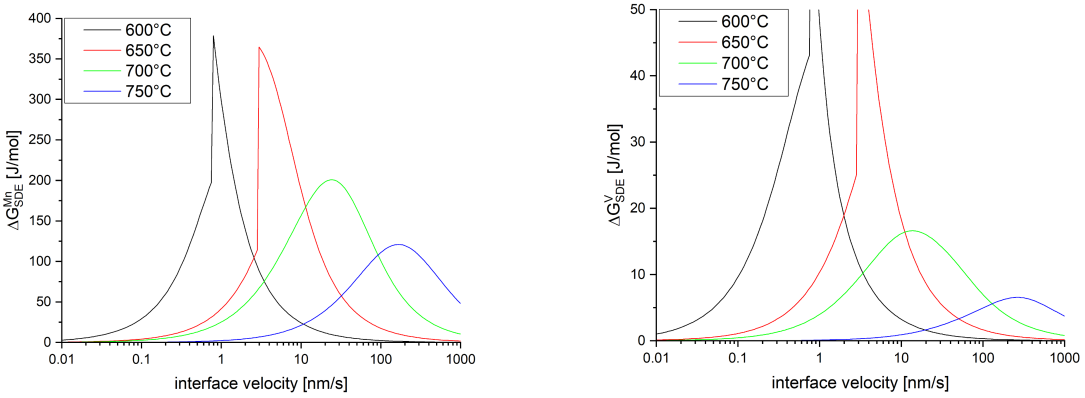

Fig. 6.5. Manganese and vanadium energy dissipation on all simulated temperatures.

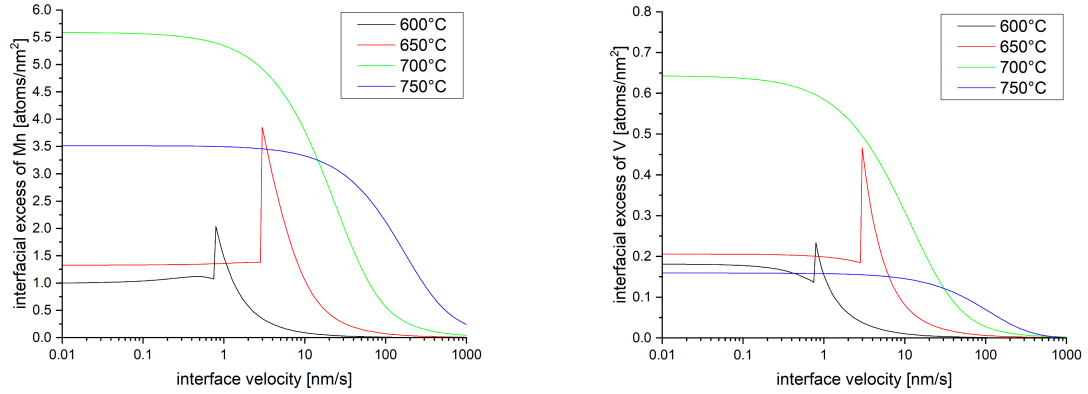

Fig. 6.6. Manganese and vanadium segregation on all simulated temperatures.

6.2.2 Effect of alloying

As stated previously, model results are shown for the LCLV alloy, with the exception presented here. **Fig. 6.7.** and **Fig. 6.8.** showcases the manganese and vanadium energy dissipation and segregation of the LCLV and HCHV alloys at 700°C. As can be seen, higher vanadium content minutely increases the energy dissipation peaks, with a higher relative change in the vanadium peak.

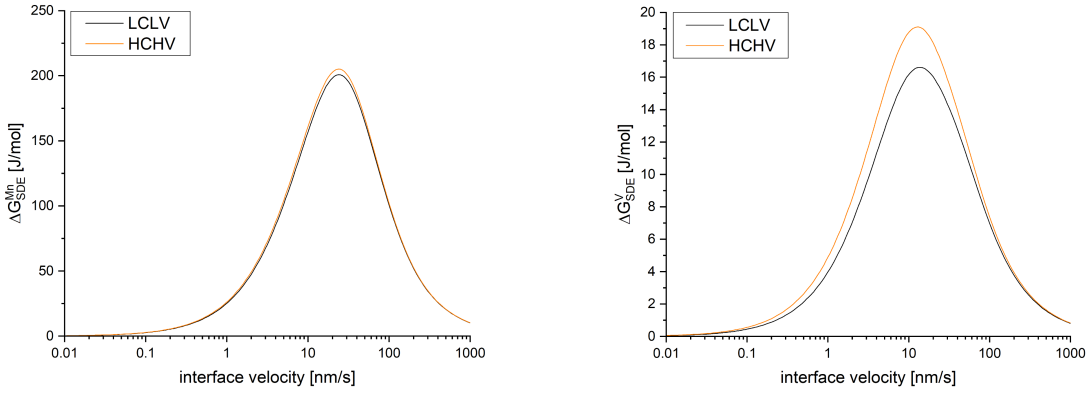

Fig. 6.7. Manganese and vanadium energy dissipation for LCLV and HCHV alloys simulated at 700°C.

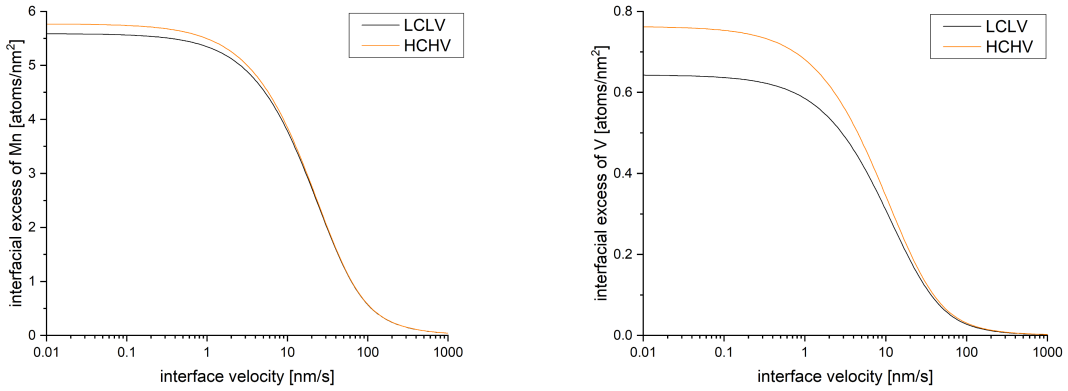

Fig. 6.8. Manganese and vanadium segregation for LCLV and HCHV alloys simulated at 700°C.

Segregation is affected in a similar manner, with slightly higher values for the higher alloyed steel. The change is more pronounced at lower interface velocities. This means that the peak of total energy dissipation will be very slightly shifted towards lower interface velocities, with an increase of alloying content as well. At lower interface velocities, elements have more time to diffuse, leading to a higher segregation.

6.2.3 Effect of interfacial diffusivity

In this simulation, the transinterfacial diffusivity D_i^{trans}, which is the diffusivity of species along the γ-α interface, is an important parameter. Yet experimentally it is hard to obtain and actual values are often not available in literature. For this reason, in present modelling the transinterfacial diffusivity has been set equal to the diffusivity of the species in ferrite, i.e. $D_i^{trans} = D_i^{\alpha}$. Alternatively, it can be chosen to use a geometric average of the diffusivity values of the species in γ and α. It has been chosen to not use a geometric average, since this just scales D_i^{α} with a factor of *1/20* to *1/10.*

Fig. 6.9. Plots the total energy dissipation of the LCLV alloy at 700°C in which $D_i^{trans} = D_i^{\alpha}$ is factored with 1/20, 1/10, 10 and 20 respectively. It can be observed that increasing the diffusivity shifts the curves towards higher interface velocities. As a result, the valleys of energy dissipation are pushed towards the region of interface friction controlled dissipation. This leads to an increase of the minimum energy dissipation during transformation.

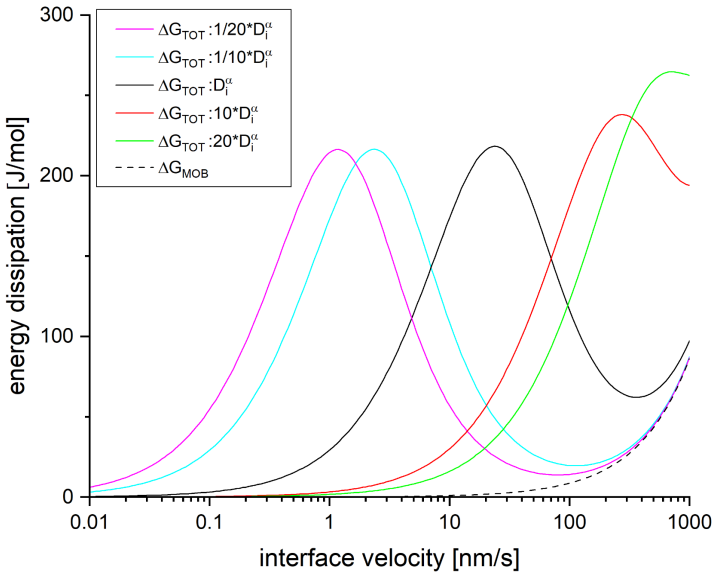

Fig. 6.9. Effect of changing transinterfacial diffusivity on ΔG_{TOT} for LCLV alloy at 700°C.

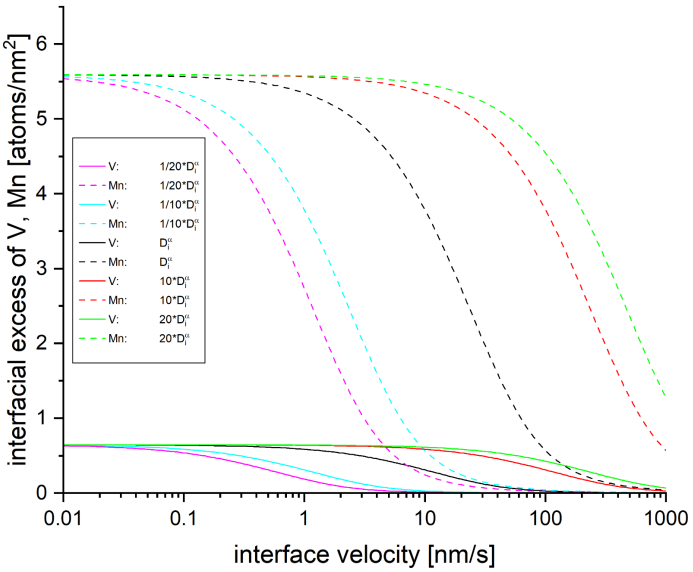

Fig. 6.10. Effect of changing transinterfacial diffusivity on interfacial excess of vanadium and manganese for LCLV alloy at 700°C.

Additionally, it can be observed in **Fig. 6.10.** that the segregation is only affected so far that reaching the steady state values obtained at low interface velocities is obtained earlier (at higher interface velocities) simply due to the solutes moving quicker through the interface.

6.2.3 Effect of mobility

Changing the pre-exponential factor of the intrinsic mobility of the interface has a great effect on the energy dissipation. Recall that the contribution of energy dissipation due to interface friction is represented by:

$$\Delta G_{MOB} = \frac{v_i}{M} \quad (6.1)$$

Where M is the intrinsic mobility of the interface. With:

$$M = M_0 e^{-Q/RT} \quad (6.2)$$

Fig. 6.11. Plots the total energy dissipation and the changing energy dissipation due to interface fraction with different values of the pre-exponential value. With a decrease of M_0 of 2.4 [34] to 0.13 mmol/sJ [35] a shift of the minimum energy dissipation during transformation towards higher values is achieved due to the higher dominance of the mobility. This corresponds with a great increase of energy dissipation due to interface friction, whose vertical asymptote is lowered towards lower interface velocities.

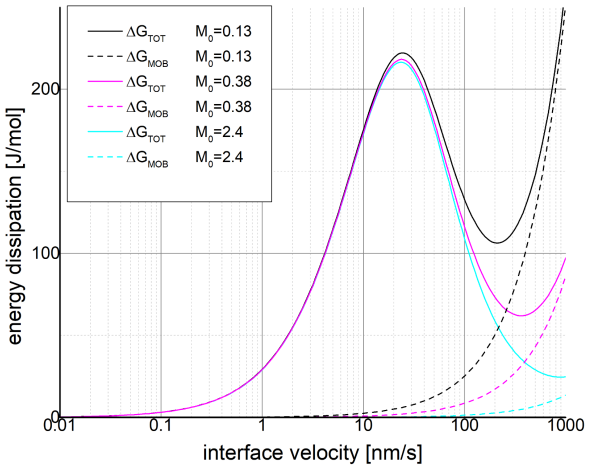

Fig. 6.11. Total energy dissipation and dissipation due to interface friction with three different pre-exponential factors.

6.2.4 Effect of manganese binding energy

A wide variety of elemental binding energies are reported in literature. The manganese binding energy to the interface has been reported to vary between 2kJ/mol and 10 kJ/mol [29], [33], [36], [37]. The elemental binding energy has a great effect on the magnitude of the energy dissipation, as can be seen in **Fig. 6.12.** Here, the modeling results are shown with E_{Mn}^{0} and 2kJ/mol and 7kJ/mol are used. A great increase of the total energy dissipation is visible due to the dominance of the manganese energy dissipation. A very slight increase in vanadium energy dissipation was observed due to the coupling of the equations.

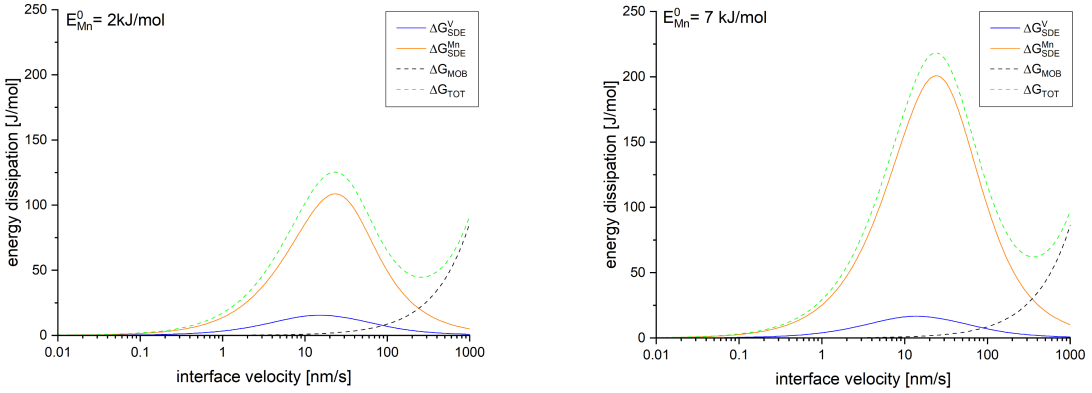

Fig. 6.12. Energy dissipation for different manganese binding energies.

6.3 Relation to experimental data and discussion

Fig. 6.13. plots the experimentally obtained peak interface velocity ranges in the modelling results for the LCLV alloy at the four analysed temperatures.

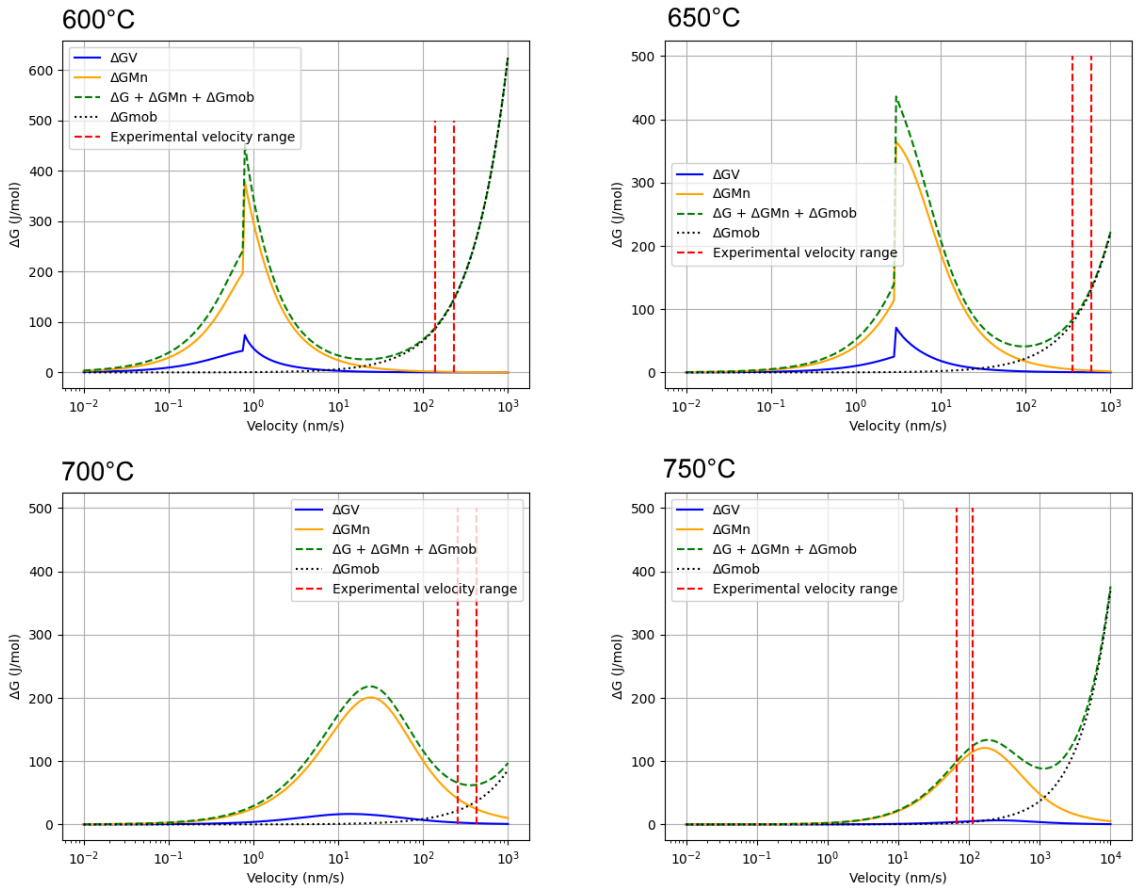

Fig. 6.13. Experimental velocity ranges (in dotted red) and modelling results for LCLV alloy.

At 600°C, the experimental interface velocity lies at the high velocity end of the well or valley of minimum energy dissipation during transformation. This is also the case for 650°C. At 700°C, the experimental velocity lies in the middle of the well. For 750°C, the experimental velocity lies past the well at the region of peak energy dissipation (after the regime change from mobility to segregation dominated).

Traditionally, in most models of interphase precipitation the idea is that when the interface slows down to sufficiently moderate velocities the solutes have time to segregate and precipitate. The regular precipitation of carbides in bands is then controlled by periodic consumption and accumulation of substitutional solutes at the migrating austenite-ferrite interface where carbon is always sufficiently around due to its high diffusivity. In many models the interface is temporarily pinned by the formed precipitates, yet those pinning forces are often overestimated.

It can also be postulated differently. When the energy dissipation increases, in this case due to manganese segregation, the precipitation of vanadium carbides would consume (excess) carbon, which would counteract the effects of manganese segregation and promote interface migration. In this case the precipitates act like a carbon sink which promotes the interface to keep migrating during transformation. The result is that a quasi-steady state of interface migration is maintained due to carbon consumption of newly formed precipitates.

In the current model results, this could be postulated by checking where the maximum interface velocity lies with respect to the need of carbon consumption with regards to the energy dissipation. In the case of 600°C and 650°C the maximum interface velocity lies substantially before the regime where there is increase in dissipation due to manganese segregation. So, after the maximum interface velocity is reached, a delay occurs and the interface velocity slows down and manganese segregation increases substantially, leading to an increased need of carbon exclusion which is accommodated by precipitation. As such, interphase precipitates are formed in this specific temperature range and interface velocity range. In the case of 700°C, the maximum experimental interface velocity lies directly at the hill of increase in energy dissipation. In this case, there is no delay for the need of carbon consumption since the right interface velocity for this temperature for precipitation and carbon consumption is already occurring. It would have to be experimentally found if VC precipitation indeed occurs without delay for this transformation temperature compared to lower temperatures. Finally, at 750°C, the experimental interface velocity range is already at the peak of energy dissipation (and possibly beyond that if the transinterface diffusivity is underestimated). This means there is less need for carbon to be excluded since no preferential energy state (to counteract the manganese energy dissipation) would be reached. This could then be a reason for why no VC interphase precipitates are found for this temperature during extensive annealing.

It must also be noted that, especially the parameters of the manganese binding energy and the transinterface diffusivity, can be fitted to improve the underlying theory. If then, these parameters can be experimentally found and checked whether they match to the best fits of the models, the underlying theory can be reinforced experimentally.

Conclusion

Modeling results have shown that the share of energy dissipation due to manganese is large relative to the total energy dissipation. This means that the differences between the experimental results of the phase transformation kinetics obtained through dilatometer experiments have to be understood in terms of vanadium segregation and precipitation behaviour, and corresponding interaction with carbon, since the manganese content in the three analysed alloys remains constant.

Energy dissipation decreases substantially with increase of transformation temperature, while the peak of energy dissipation during transformation is shifted towards higher interface velocities. An increase of selected transinterface diffusivity likewise shifts the peak towards higher interface velocities. A result is an increase of the minimum energy dissipation well during transformation due to the dominant energy dissipation due to interface friction at high interface velocities. Only a very small difference between the modelling results of the different alloys is found, this can again be understood due to the dominance of the manganese in the energy dissipation, whose elemental content is the same for the different analysed alloys.

Experimental results vary greatly. When categorised per annealing temperature the following observations are made:

- At 600°C a large retardation of the transformation of the LCLV alloy is observed, or to be put differently, a large increase of transformation kinetics for BASE and HCHV alloys is seen.
- At 650°C the phase transformation follows more traditionally expected orders. BASE alloy transforms the fastest, followed by LCLV and then HCHV. The increase of alloying supposedly decreases the phase transformation.
- At 700°C a large retardation of the BASE alloy is observed. LCLV transforms the fastest, followed closely by HCHV. It is not known why BASE alloy transforms slower, but an artifact of dilatometry is not excluded.
- At 750°C the phase transformations were not completed in the 4 hours of annealing. All alloys showcase an extension and retraction of the sample in the initial part of annealing, leading to a bump in the transformed fraction. It is not known what causes this, but likely true transformation initiates after initial retraction. From there, the BASE alloy transforms fastest, followed closely by the LCLV and HCHV samples.

When categorised per alloy type the following observations are made:

- For the BASE alloy, annealing at 600°C transforms the fastests, followed quickly by 650°C. At 700°C the transformation is substantially slower, and afterwards followed by 750°C if the initial bump is omitted.
- For the LCLV alloy, annealing at 650°C now transforms the fastest, followed by 700°C and then by 600°C. Again if the initial bump is omitted, at 750°C the transformation is slowest.
- For the HCHV alloy, initial transformation at 600°C is most rapid, as was for the BASE alloy. Full transformation is not reached after 1 hour of annealing however, and after ca. 120 seconds transformation is overtaken by 650°C and 700°C, which transform very similarly, and initially thus slower. At 750°C, the transformation is slowest, regardless if the initial bump is taken into consideration or not.

When plotting the experimentally obtained peak interface velocity range onto the modelling results the following observations can be made. At lower transformation temperatures, the velocity range lies before or just in the region of minimum energy dissipation. Here, energy dissipation is still expected to decrease or remain constant for a short range of decrease of interface velocity. An increase of transformation temperature then shifts the velocity range towards the onset of increase of energy dissipation, i.e. the start of the slope towards the peak energy dissipation during transformation. At the highest transformation temperature of 750°C, the velocity range lies at, or just past, the peak energy dissipation, highly dependent on among others the selected transinterface diffusivity.

A theory is then postulated as follows. When the energy dissipation increases, in this case due to manganese segregation, the precipitation of vanadium carbides would consume (excess) carbon, which would promote interface migration and counteract the effects of manganese segregation. In this case the precipitates act like a carbon sink which promotes the interface to keep migrating during transformation. The result is that a quasi-steady state of interface migration is maintained due to carbon consumption of newly formed precipitates. In the case of 600°C and 650°C the maximum interface velocity lies substantially before the increase in dissipation due to manganese segregation. So, after the maximum interface velocity is reached, a delay occurs and the interface velocity slows down and manganese segregation increases substantially, leading to an increased need of carbon exclusion which is accommodated by precipitation. In the case of 700°C, the maximum experimental interface velocity lies directly at the hill of increase in energy dissipation. In this case, there is no delay for the need of carbon consumption since the right interface velocity for this temperature for precipitation and carbon consumption is already occurring. Finally, at 750°C, the experimental interface velocity range is already at the peak of energy dissipation (and possibly beyond that if the transinterface diffusivity is underestimated). This means there is less need for carbon to be excluded since no preferential energy state (to counteract the manganese energy dissipation) would be reached. This could then be a reason for why no VC interphase precipitates are found for this temperature during extensive annealing.

References

[1] P. Li and J. A. Todd, 'Application of a new model to the interphase precipitation reaction in vanadium steels', *Metall. Trans. A*, vol. 19, no. 9, pp. 2139–2151, Sep. 1988, doi: 10.1007/BF02645039.

[2] D. Raabe *et al.*, 'Current Challenges and Opportunities in Microstructure-Related Properties of Advanced High-Strength Steels', *Metall. Mater. Trans. A*, vol. 51, no. 11, pp. 5517–5586, Nov. 2020, doi: 10.1007/s11661-020-05947-2.

[3] R. Lagneborg and S. Zajac, 'A model for interphase precipitation in V-microalloyed structural steels', *Metall. Mater. Trans. A*, vol. 32, no. 1, pp. 39–50, Jan. 2001, doi: 10.1007/s11661-001-0249-9.

[4] I. Bikmukhametov, H. Beladi, J. Wang, P. D. Hodgson, and I. Timokhina, 'The effect of strain on interphase precipitation characteristics in a Ti-Mo steel', *Acta Mater.*, vol. 170, pp. 75–86, May 2019, doi: 10.1016/j.actamat.2019.03.022.

[5] J. Byggmästar, M. Nagel, K. Albe, K. O. E. Henriksson, and K. Nordlund, 'Analytical interatomic bond-order potential for simulations of oxygen defects in iron', *J. Phys. Condens. Matter*, vol. 31, no. 21, p. 215401, May 2019, doi: 10.1088/1361-648X/ab0931.

[6] Z. Xiong, I. Timokhina, and E. Pereloma, 'Clustering, nano-scale precipitation and strengthening of steels', *Prog. Mater. Sci.*, vol. 118, p. 100764, May 2021, doi: 10.1016/j.pmatsci.2020.100764.

[7] M. Gouné *et al.*, 'Overview of the current issues in austenite to ferrite transformation and the role of migrating interfaces therein for low alloyed steels', *Mater. Sci. Eng. R Rep.*, vol. 92, pp. 1–38, Jun. 2015, doi: 10.1016/j.mser.2015.03.001.

[8] M. Militzer, C. Hutchinson, H. Zurob, and G. Miyamoto, 'Modelling of the diffusional austenite-ferrite transformation', *Int. Mater. Rev.*, vol. 68, no. 7, pp. 725–754, Oct. 2023, doi: 10.1080/09506608.2022.2126257.

[9] Y.-J. Zhang, E. Chandiran, H.-K. Dong, N. Kamikawa, G. Miyamoto, and T. Furuhara, 'Current Understanding of Microstructure and Properties of Micro-Alloyed Low Carbon Steels Strengthened by Interphase Precipitation of Nano-Sized Alloy Carbides: A Review', *JOM*, vol. 73, no. 11, pp. 3214–3227, Nov. 2021, doi: 10.1007/s11837-021-04882-w.

[10] Y.-J. Zhang, G. Miyamoto, K. Shinbo, and T. Furuhara, 'Effects of α/γ orientation relationship on VC interphase precipitation in low-carbon steels', *Scr. Mater.*, vol. 69, no. 1, pp. 17–20, Jul. 2013, doi: 10.1016/j.scriptamat.2013.03.020.

[11] J. Sietsma and S. Van Der Zwaag, 'A concise model for mixed-mode phase transformations in the solid state', *Acta Mater.*, vol. 52, no. 14, pp. 4143–4152, Aug. 2004, doi: 10.1016/j.actamat.2004.05.027.

[12] H. K. D. H. Bhadeshia, 'Considerations of solute-drag in relation to transformations in steels', *J. Mater. Sci.*, vol. 18, no. 5, pp. 1473–1481, May 1983, doi: 10.1007/BF01111967.

[13] M. Hillert, 'Solute drag in grain boundary migration and phase transformations', *Acta Mater.*, vol. 52, no. 18, pp. 5289–5293, Oct. 2004, doi: 10.1016/j.actamat.2004.07.032.

[14] L. Himmel, *Recovery and Recrystallization of Metals, Proceedings of a Symposium held in New York*, 1st edn. New York: Interscience Publishers, 1963.

[15] J. W. Cahn, 'The impurity-drag effect in grain boundary motion', *Acta Metall.*, vol. 10, no. 9, pp. 789–798, Sep. 1962, doi: 10.1016/0001-6160(62)90092-5.

[16] M. Hillert and B. Sundman, 'A treatment of the solute drag on moving grain boundaries and phase interfaces in binary alloys', *Acta Metall.*, vol. 24, no. 8, pp. 731–743, Aug. 1976, doi: 10.1016/0001-6160(76)90108-5.

[17] G. R. Purdy and Y. J. M. Brechet, 'A solute drag treatment of the effects of alloying elements on the rate of the proeutectoid ferrite transformation in steels', *Acta Metall. Mater.*, vol. 43, no. 10, pp. 3763–3774, Oct. 1995, doi: 10.1016/0956-7151(95)90160-4.

[18] M. Hillert, J. Odqvist, and J. Ågren, 'Comparison between solute drag and dissipation of Gibbs energy by diffusion', *Scr. Mater.*, vol. 45, no. 2, pp. 221–227, Jul. 2001, doi: 10.1016/S1359-6462(01)01022-3.
[19] M. Enomoto, 'Influence of solute drag on the growth of proeutectoid ferrite in Fe–C–Mn alloy', *Acta Mater.*, vol. 47, no. 13, pp. 3533–3540, Oct. 1999, doi: 10.1016/S1359-6454(99)00232-3.
[20] J. Odqvist, M. Hillert, and J. Ågren, 'Effect of alloying elements on the γ to α transformation in steel. I', *Acta Mater.*, vol. 50, no. 12, pp. 3213–3227, Jul. 2002, doi: 10.1016/S1359-6454(02)00143-X.
[21] C. Ioannidou *et al.*, 'Interaction of precipitation with austenite-to-ferrite phase transformation in vanadium micro-alloyed steels', *Acta Mater.*, vol. 181, pp. 10–24, Dec. 2019, doi: 10.1016/j.actamat.2019.09.046.
[22] J. Collins, M. Taylor, A. L. Scarlett, E. J. Palmiere, and E. J. Pickering, 'Prior austenite grain measurement: A direct comparison of EBSD reconstruction, thermal etching and chemical etching', *Mater. Charact.*, vol. 208, p. 113656, Feb. 2024, doi: 10.1016/j.matchar.2024.113656.
[23] C. García De Andrés, M. J. Bartolomé, C. Capdevila, D. San Martín, F. G. Caballero, and V. López, 'Metallographic techniques for the determination of the austenite grain size in medium-carbon microalloyed steels', *Mater. Charact.*, vol. 46, no. 5, pp. 389–398, May 2001, doi: 10.1016/S1044-5803(01)00142-5.
[24] C. Ioannidou *et al.*, 'Evolution of the precipitate composition during annealing of vanadium micro-alloyed steels by in-situ SANS', *Acta Mater.*, vol. 201, pp. 217–230, Dec. 2020, doi: 10.1016/j.actamat.2020.09.083.
[25] C. Ioannidou *et al.*, 'Phase-transformation and precipitation kinetics in vanadium micro-alloyed steels by in-situ, simultaneous neutron diffraction and SANS', *Acta Mater.*, vol. 220, p. 117317, Nov. 2021, doi: 10.1016/j.actamat.2021.117317.
[26] J. Trzaska, 'Empirical Formulae for The Calculation of Austenite Supercooled Transformation Temperatures', *Arch. Metall. Mater.*, vol. 60, no. 1, pp. 181–185, Apr. 2015, doi: 10.1515/amm-2015-0029.
[27] J. Trzaska, 'Calculation of Critical Temperatures by Empirical Formulae', *Arch. Metall. Mater.*, vol. 61, no. 2, pp. 981–986, Jun. 2016, doi: 10.1515/amm-2016-0167.
[28] Z. Zhao, C. Liu, Y. Liu, and D. O. Northwood, 'A new empirical formula for the bainite upper temperature limit of steel', *J. Mater. Sci.*, vol. 36, no. 20, pp. 5045–5056, Oct. 2001, doi: 10.1023/A:1011874708194.
[29] G. Miyamoto, K. Yokoyama, and T. Furuhara, 'Quantitative analysis of Mo solute drag effect on ferrite and bainite transformations in Fe-0.4C-0.5Mo alloy', *Acta Mater.*, vol. 177, pp. 187–197, Sep. 2019, doi: 10.1016/j.actamat.2019.07.040.
[30] M. Hillert and L.-I. Staffansson, 'The Regular Solution Model for Stoichiometric Phases and Ionic Melts.', *Acta Chem. Scand.*, vol. 24, pp. 3618–3626, 1970, doi: 10.3891/acta.chem.scand.24-3618.
[31] B. Sundman and J. Ågren, 'A regular solution model for phases with several components and sublattices, suitable for computer applications', *J. Phys. Chem. Solids*, vol. 42, no. 4, pp. 297–301, Jan. 1981, doi: 10.1016/0022-3697(81)90144-X.
[32] J. Zhu, H. Luo, Z. Yang, C. Zhang, S. Van Der Zwaag, and H. Chen, 'Determination of the intrinsic α/γ interface mobility during massive transformations in interstitial free Fe-X alloys', *Acta Mater.*, vol. 133, pp. 258–268, Jul. 2017, doi: 10.1016/j.actamat.2017.05.045.
[33] S. Clark, V. Janik, Y. Lan, and S. Sridhar, 'Interphase Precipitation – An Interfacial Segregation Model', *ISIJ Int.*, vol. 57, no. 3, pp. 524–532, 2017, doi: 10.2355/isijinternational.ISIJINT-2016-544.
[34] J. J. Wits, T. A. Kop, Y. Van Leeuwen, J. Seitsma, and S. Van Der Zwaag, 'A study on the austenite-to-ferrite phase transformation in binary substitutional iron alloys', *Mater. Sci. Eng. A*, vol. 283, no. 1–2, pp. 234–241, May 2000, doi: 10.1016/S0921-5093(00)00735-8.

[35] H. Dong, Y. Zhang, G. Miyamoto, H. Chen, Z. Yang, and T. Furuhara, 'A comparative study on intrinsic mobility of incoherent and semicoherent interfaces during the austenite to ferrite transformation', *Scr. Mater.*, vol. 188, pp. 59–63, Nov. 2020, doi: 10.1016/j.scriptamat.2020.07.007.
[36] T. Jia and M. Militzer, 'Modelling Phase Transformation Kinetics in Fe–Mn Alloys', *ISIJ Int.*, vol. 52, no. 4, pp. 644–649, 2012, doi: 10.2355/isijinternational.52.644.
[37] A. T. Wicaksono and M. Militzer, 'Interaction of C and Mn in a ∑3 grain boundary of bcc iron', *IOP Conf. Ser. Mater. Sci. Eng.*, vol. 219, p. 012044, Jul. 2017, doi: 10.1088/1757-899X/219/1/012044.
[38] H. Takada, 'Alloy Designing of High Strength Bainite Steels for Hot Forging', *Tetsu--Hagane*, vol. 88, no. 9, pp. 534–538, 2002, doi: 10.2355/tetsutohagane1955.88.9_534.

Appendix

A1. Calculations bainite starting temperature

Tab. A1.1 (3.1.). Chemical composition used alloys

Sample		C	V	Mn	Si	S	Al	Fe
BASE	wt. %	0.068	0.001	1.792	0.018	0.0008	0.022	bal.
LCLV	wt. %	0.068	0.285	1.790	0.008	0.0013	0.035	bal.
HCHV	wt. %	0.138	0.609	1.790	0.011	0.0012	0.036	bal.

Takada [38]:

$$B_S = 1336 - 1446x_C - 62.3x_{Mn} - 36.5x_{Si} - 47.8x_{Cr} - 160x_V - 77.5x_{Mo}$$

$$B_S = 1336 - 1446x_C - 62.3x_{Mn} - 36.5x_{Si} - 160x_V$$

Trzaska 1 [26]:

$$B_S = 675 - 212x_C - 57x_{Mn} - 17x_{Si} - 29x_{Ni} - 49x_{Cr} - 60x_{Mo} - 94x_V + 0.056T_a - 1.6v_r^{0.25}$$

$$B_S = 675 - 212x_C - 57x_{Mn} - 17x_{Si} - 94x_V + 0.056T_a - 1.6v_r^{0.25}$$

T_a: annealing temperature [°C] $= 1100$

v_r: cooling rate [°C/min] $= 900$

Trzaska 2 [27]:

$$B_S = 771 - 231.5x_C - 69x_{Mn} - 23x_{Si} - 58.5x_{Cr} - 31x_{Ni} - 55x_{Mo} - 41x_V$$

$$B_S = 771 - 231.5x_C - 69x_{Mn} - 23x_{Si} - 41x_V$$

Zhao 2 [28]:

$$B_S = 640 - 45x_{Mn} - 40x_V - 35x_{Si} - 30x_{Cr} - 25x_{Mo} - 20x_{Ni} - 15x_W$$

$$B_S = 640 - 45x_{Mn} - 40x_V - 35x_{Si}$$

Tab. A1.2. (4.1.) Calculated bainite start temperatures B_S .

BASE [°C]	LCLV [°C]	HCHV [°C]	Ref.
1125	1080	927.1	[38]
610.9	584.5	539.1	[26]
631.2	619.9	590.3	[27]
558.7	547.8	534.7	[28]

A2. Stability analysis

In this chapter, the instability of the solute drag model at low temperature for certain interface velocities is analysed.

A2.1 Parametric analysis

A2.1.1 Shape of potential well

To check if the discontinuity introduced in the piecewise triangular potential wells affects the instability of the numerical results a different parabolic potential well was introduced. The original (used in all other model results) and new parabolic wells are visualised in **Fig. A2.1.**

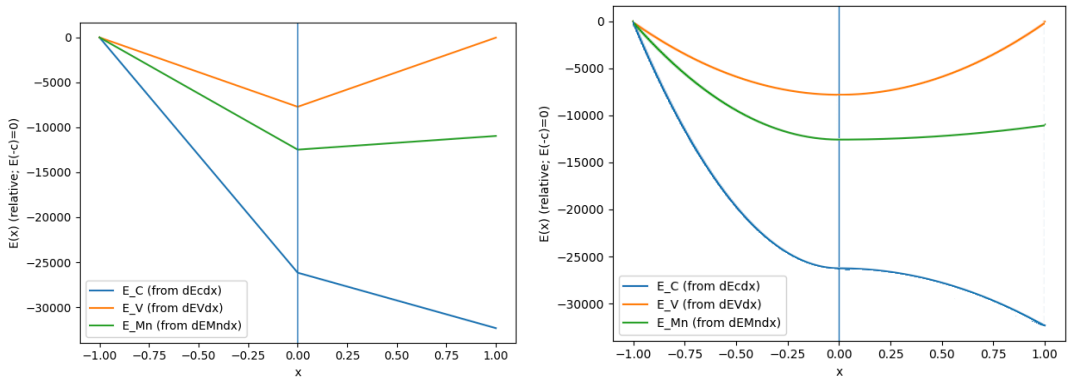

Fig. A2.1. Triangular and parabolic shaped potential wells.

The model was run with these new potential wells and no stability improvements were found, as seen in **Fig A2.2**. It can be concluded that the discontinuity has no effect on the stability, and the instability is solely resultant on the actual magnitudes of the relevant input parameters.

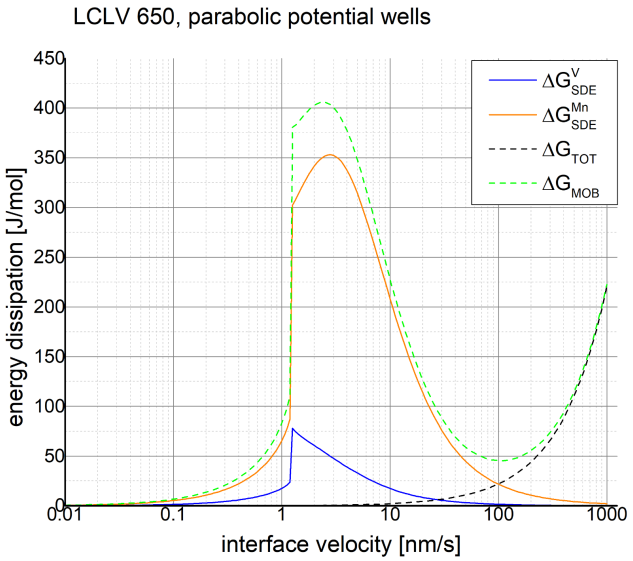

Fig. A2.2. Energy dissipation for LCLV at 650°C using parabolic potential wells.

A2.2 Mathematical analysis

The analysed system of non-linear ordinary differential equations is not solved in the explicit form of $dy/dx = f(x, y)$ but in an implicit form:

(A2.1) $M(x, y)\frac{dy}{dx} = r(x, y)$

Where $M(x, y)$ is the so called mass-matrix and $r(x, y)$ is the right-hand side. Numerically it is converted to explicit form at each evaluation by solving:

(A2.2) $\frac{dy}{dx} = F(x, y) := M(x, y)^{-1} r(x, y)$

At this inversion step is where crucial numerical stability diagnostics can be ascertained.

A2.2.1 Mass matrix determinant

The determinant can be used as a singularity detector. When the determinant is unequal to 0, the matrix is invertible and the explicit vector field $F(x, y) = M^{-1} r$ is properly defined. When the determinant becomes 0, the mass matrix is singular and the ODE system becomes degenerate, i.e.:

$det(M) \neq 0$	$\rightarrow$	M is invertible	$\rightarrow$	non-singular behaviour
$det(M) = 0$	$\rightarrow$	M is non-invertible	$\rightarrow$	singular behaviour

When the determinant approaches 0 or $det(M) \sim 0$, at least one eigenvector of M tends to zero:

(A2.3) $\exists \lambda_{min}(M) \rightarrow 0$

Inverting M creates a factor of $1/\lambda_{min}$, so the vector field magnitude can blow up even if the right hand side of the system is moderate:

(A2.4) $||F|| = \left|\left|M^{-1} r\right|\right| \leq \left|\left|M^{-1}\right|\right| \cdot ||r||$

A norm operator compatible with the Euclidean norm, or the spectral norm of the mass matrix is:

(A2.5) $\left|\left|M^{-1}\right|\right|_2 = \frac{1}{\sigma_{min}(M)}$

Where $\sigma_{min}(M)$ is the smallest singular eigenvalue. Thus if $\sigma_{min}(M)$ is tiny, $\left|\left|M^{-1}\right|\right|$ is huge and you get enormous derivatives, increased sensitivity to perturbations and possibilities of numerical blow-ups. The magnitude of the determinant thus indicates at least one near-zero singular value, which makes the inversion required in solving the system of equations unstable.

The system of ODE and corresponding mass-matrix was analysed using Python. **Fig. A2.3.** shows $\sigma_{min}(M)$ plotted against v_i for the case of the LCLV alloy at 650° around the instability turnover point found at 3 nm/s . It can be seen that at low velocities, the determinant

reaches extremely small values of around 10^{-7} to 10^{-8} before blowing up several orders of magnitude to around $10^{0} = 1$.

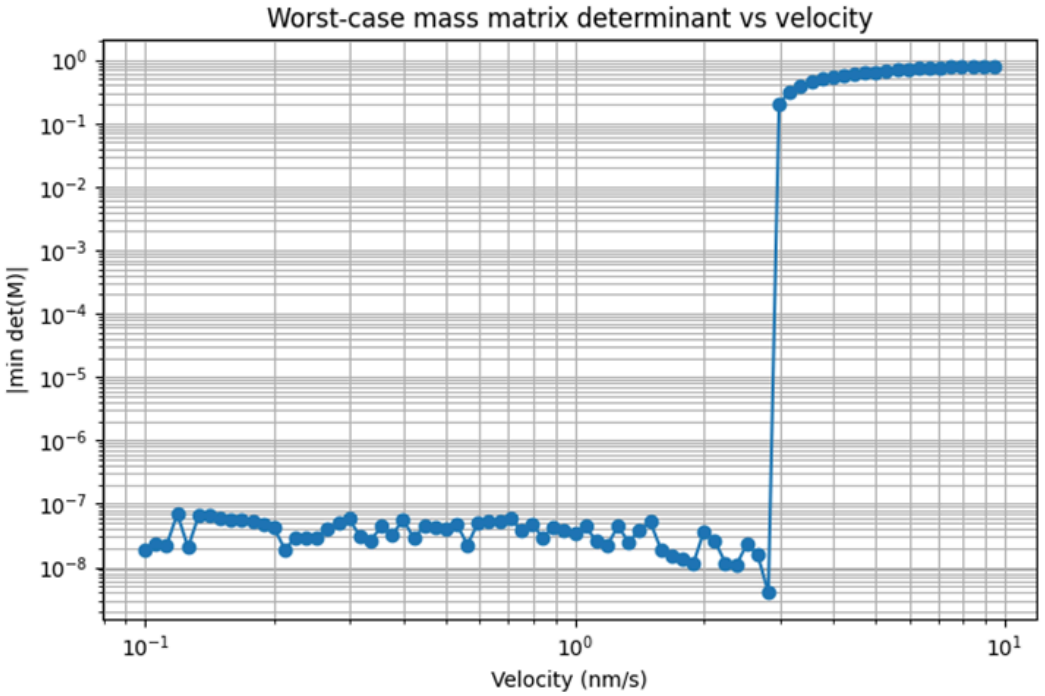

Fig. A2.3. Worst case $det(M)$ around the interface velocity where instability was found. In this case LCLV 650°C, with the spike around a velocity of 3 nm/s.

The mass matrix is defined as:

$$M = \begin{bmatrix} 1 & g_1 & g_2 \\ g_3 & 1 - y_2 & y_1 \\ g_6 & y_2 & 1 - y_1 \end{bmatrix}$$

with

$$g_1 = e y_0 (1 - y_0)$$
$$g_2 = f y_0 (1 - y_0)$$
$$g_3 = e y_1 (1 - y_1 - y_2)$$
$$g_6 = f y_2 (1 - y_1 - y_2)$$

Where e and f are constants (the Wagner interaction parameters).

Because the top-left entry is 1, the matrix can be written in block form:

$$M = \begin{bmatrix} 1 & u^T \\ v & B \end{bmatrix}$$

Where:

$$u^T = \begin{bmatrix} g_1 & g_2 \end{bmatrix}$$

$$v = \begin{bmatrix} g_3 \\ g_6 \end{bmatrix}$$

And:

$$B = \begin{bmatrix} 1 - y_2 & y_1 \\ y_2 & 1 - y_1 \end{bmatrix}$$

Using the Schur complement identity, the determinant of *M* becomes:

(A2.6) $det(M) = det(B - vu^T)$

Thus the determinant of the full matrix depends on the effective matrix S:

(A2.7) $S = B - vu^T$

This is useful because it separates the mass matrix into a baseline matrix B and a rank-1 correction vu^T.
The determinant of *B* is:

(A2.8) $det(B) = (1 - y_2)(1 - y_1) - y_1 y_2 = 1 - y_1 - y_2$

This shows that the baseline matrix becomes singular when $y_1 + y_2 = 1$. This corresponds to a physical boundary in the composition space. Thus the determinant diagnostic is directly connected to a physical constraint surface in the system.

Even if $1 - y_1 - y_2$ is not small, the term vu^T can cause cancellation. The correction matrix is then defined as:

$$vu^T = \begin{bmatrix} g_3 g_1 & g_3 g_2 \\ g_6 g_1 & g_6 g_2 \end{bmatrix}$$

Substituting the expressions for g_i.
These terms involve products such as:

(7.9) $y_0(1-y_0)y_1(1-y_1-y_2)$ and $y_0(1-y_0)y_2(1-y_1-y_2)$

Therefore the determinant can become small through two main mechanisms:

Mechanism (i): boundary singularity:

$y_1 + y_2 \to 1$

Which makes *B* singular.

Mechanism (ii): cancellation:

$\left||vu^T|\right| \sim ||B||$

This occurs when the non-linear coupling terms are large enough to the baseline block.

A2.2.2 Mass matrix condition

In the 2-norm;

(A2.10) $$K_2(M) = ||M||_2 \left|M^{-1}\right|_2 = \frac{\sigma_{max}(M)}{\sigma_{min}(M)}$$

Or:

(A2.11) $$\kappa(M(x, y(x)) = \frac{\sigma_{max}(M(x, y(x)))}{\sigma_{min}(M(x, y(x)))}$$

This is a measure of the sensitivity of $M\,z = b$ to small perturbations.

As mentioned earlier, every time the solver evaluates $F(x, y)$, it solves:

(A2.12) $$M(x, y)z = r(x, y), \quad z = dy/dx(x)$$

Suppose due to a floating point error or non linear iteration error a slightly perturbed system is solved:

(A2.13) $$(M + \delta M)(z + \delta z) = r + \delta r$$

A standard perturbation results says to first order:

(A2.14) $$\frac{||\delta z||}{||z||} \leq \kappa(M)\left(\frac{||\delta M||}{||M||} + \frac{||\delta r||}{||r||}\right)$$

So $\kappa(M)$ is an amplifier, it multiplies whatever tiny errors that are present in evaluating the mass matrix M and right hand side r, and turns them into large errors in the derivative dy/dx.

Even if $\kappa(M)$ is large but smooth, a stiff solver as used presently, can often adopt by using smaller step sizes. But if the condition number spikes sharply in x (or as a function of the velocity) then the numerical vector field changes greatly in a small region, and in addition the step size control can become erratic.

Mathematically, if $\sigma_{min}(M)$ drops sharply, then the inverse of the mass matrix M^{-1} changes rapidly and thus $F = M^{-1}r$ becomes highly unsmooth even if r is smooth. For the model in question, the most practical fact is:

(A2.14) $$||F(x,y)|| = \left|\left|M^{-1}r\right|\right| \leq \left|\left|M^{-1}\right|\right| ||r|| = \frac{||r||}{\sigma_{min}(M)}$$

So even if the right hand side is normal, if $\sigma_{min}(M)$ is tiny, the derivative dy/dx becomes large. **Fig. A2.4**. highlights the worst case mass matrix condition number, i.e. $\kappa_{worst}(v) = max\ \kappa(M)$ plotted against v_i for the case of the LCLV alloy at 650° around the instability turnover point found at 3 nm/s . Again, around the same instability point, a massive drop and change in order of magnitudes can be observed.

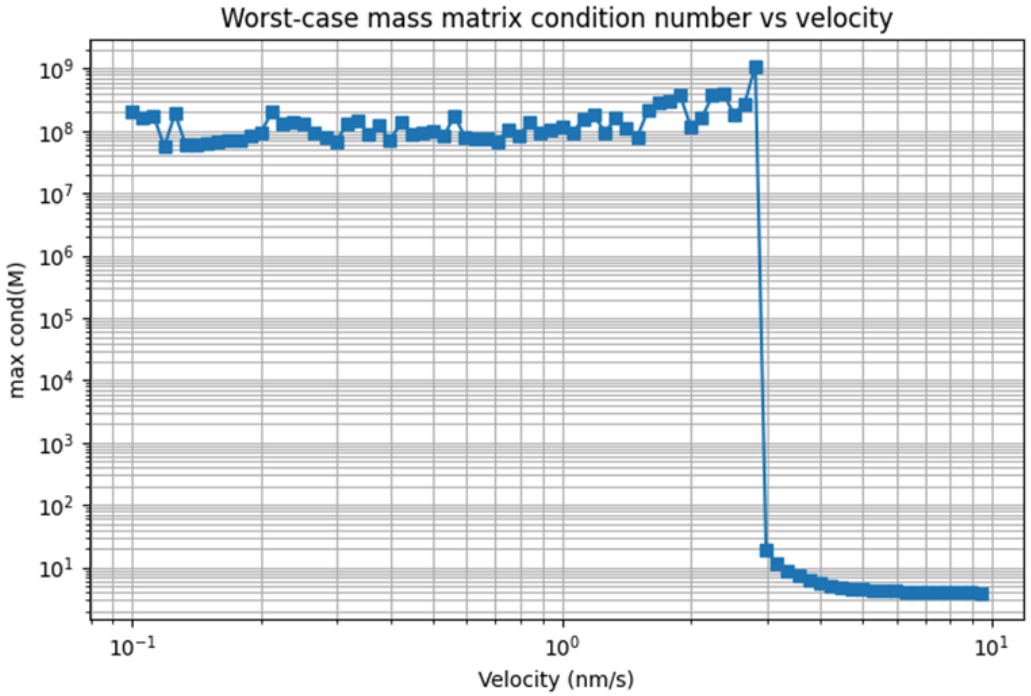

Fig. A2.4. Worst case $\kappa(M)$ around the interface velocity where instability was found. In this case LCLV 650°C, with the spike around a velocity of 3 nm/s.

A2.2.3 Mass matrix Jacobian spectral radius

Here the Jacobian is for the explicit vector field:

(A2.15) $$F(x,y) = M(x,y)^{-1}r(x,y)$$

and

(A2.16) $J(x, y) = \frac{\partial F}{\partial y}(x, y)$

And the spectral radius is defined as the largest magnitude of the eigenvalues of the Jacobian:

(A2.17) $\rho(J) = max_i \left|\lambda_i(J)\right|$

Where $\lambda_i(J)$ are the eigenvalues of J. The spectral radius relates to stability and stiffness.
If the system of ODE is linearised around a trajectory $y(x)$, a perturbation δy evolves as:

(A2.18) $\frac{d}{dx}\delta y = J(x,\ y(x))\delta y$

If J were constant, the solution is:

(A2.19) $\delta y(x) = e^{J(x-x_0)}\delta y(x_0)$

The real parts of the eigenvalues of J control how perturbations evolve, and are actually the proper stability criteria. However, the magnitudes of the eigenvalues, $\rho(J)$ are excellent stability proxies. They tell the strongest local dynamical amplification (or stiffness) encountered anywhere in the system. If $|\lambda|$ is large, there are fast time and space scales. This means that explicit solvers require very small stepsizes, and implicit solvers, like the one used presently, can handle it, but require more work per step.

This means that the spectral radius is essentially a system stiffness indicator. High values of $|\lambda|$ increase the computational burden because Newton systems become harder to solve and error control enforces smaller steps. A rapid change in $\rho(J)$ across velocity can entail that a potential regime change or degeneration of the computed Jacobian is happening.

The Jacobian for the current system can be derived as follows:

(A2.20) $F = M^{-1}r$

(A2.21) $dF = d(M^{-1})r + M^{-1}dr$

Where the following identity can be used:

(A2.22) $d(M^{-1}) = -M^{-1}(dM)M^{-1}$

Thus:

(A2.23) $dF = -M^{-1}(dM)M^{-1}r + M^{-1}(dr)$

Since $M^{-1}r = F$, the following is obtained:

(A2.24) $dF = M^{-1}(dr - (dM)F)$

Turning this into a Jacobian:

(A2.25) $$J = \frac{\partial F}{\partial y} = M^{-1}\left(\frac{\partial r}{\partial y} - \frac{\partial M}{\partial y}F\right)$$

In this formula it can be seen how the mass matrix affects stiffness. If M is near singular, M^{-1} is huge, J can become huge even if $\partial r/\partial y$ is moderate. If $\partial M/\partial y$ is large, the second term can dominate and create large eigenvalues.

This formula shows two important things specific to the equations of the system:

(a) A near singular M makes J go to high values.

Because J has the inverse mass matrix M^{-1} in front:

(A2.26) $$||J|| \lesssim \left|\left|M^{-1}\right|\right|\left(\left|\left|\frac{\partial r}{\partial y}\right|\right| + \left|\left|\frac{\partial M}{\partial y}\right|\right||F||\right)$$

And because:

(A2.27) $$||F|| \leq \frac{||r||}{\sigma_{min}(M)}$$

This leads to:

(A2.28) $$||J|| \leq \frac{1}{\sigma_{min}(M)}\left|\left|\frac{\partial r}{\partial y}\right|\right| + \frac{1}{\sigma_{min}(M)^2}\left|\left|\frac{\partial M}{\partial y}\right|\right||r||$$

If $\sigma_{min}(M)$ is tiny, $\left|\left|M^{-1}\right|\right|$ is huge, and J can become enormous. Additionally, $\frac{1}{\sigma_{min}(M)^2}$ scales even faster than the derivative itself.

(b) The right hand side r has built in stiff linear relaxation terms.

The right hand side contains terms like:

$$-\frac{v_i}{D_V^{\alpha}}(y_V - y_V^0), \qquad -\frac{v_i}{D_{Mn}^{\alpha}}(y_{Mn} - y_{Mn}^0)$$

Thus:

$$\frac{\partial r_2}{\partial y_V^0} \sim -\frac{v_i}{D_V^{\alpha}}, \qquad \frac{\partial r_3}{\partial y_{Mn}^0} \sim -\frac{v_i}{D_{Mn}^{\alpha}}$$

As b increases, these derivatives grow in magnitude. This naturally increases the size of the Jacobian unless something else changes. So $\rho(J)$ is capturing different things. The stiffness from the relaxation scale set by v/D, the stiffness amplification from M^{-1} and additional stiffness from the state-dependance in M.

Figure A2.5. highlights the worst case Jacobian spectral radius i.e. the maximum values, plotted against v_i for the case of the LCLV alloy at 650° around the instability turnover point found at 3 nm/s. Again, around the same instability point, a massive drop and change in order of magnitudes can be observed, indicating massive instabilities.

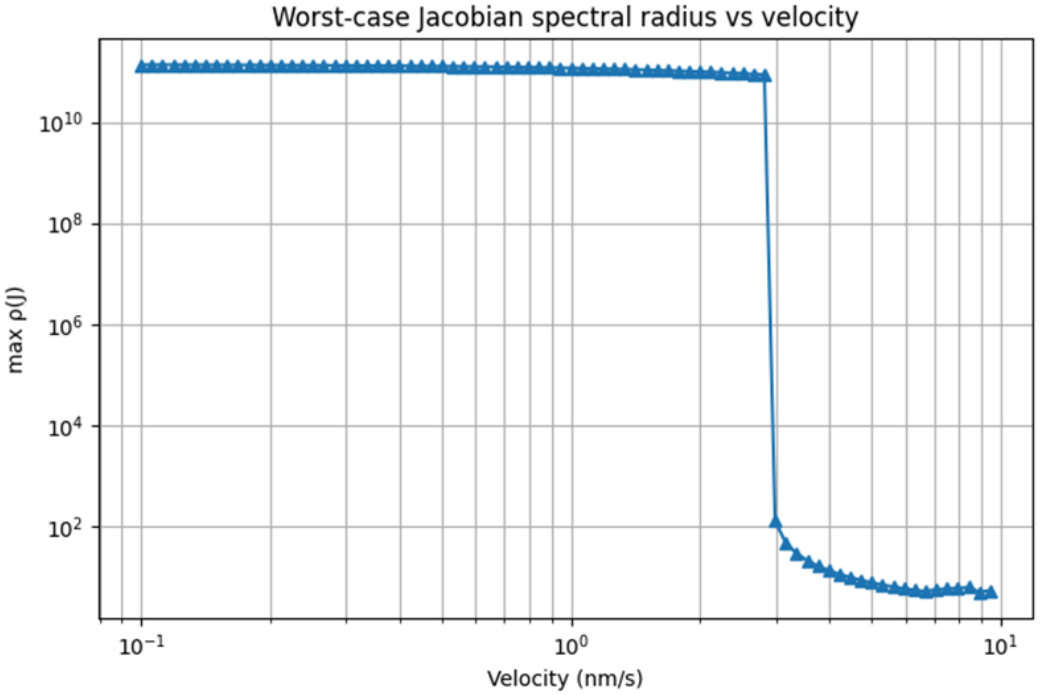

Fig. A2.5. Worst case $\rho(J)$, i.e. max value, around the interface velocity where instability was found. In this case LCLV 650°C, with the spike around a velocity of 3 nm/s.

Summarising, the diagnostic show that; $det(M)$ detects when $\sigma_{min}(M) \to 0$ and shows whether the mass matrix is approaching singularity, $\kappa(M)$ measures $\sigma_{max}/\sigma_{min}$ and tells how small $\sigma_{min}(M)$ is relative to the other singular values. A large $\kappa(M)$ implies a large $\left\|M^{-1}\right\|$ which leads to $dy/dx = M^{-1}r$ becoming extremely large. Finally, $\rho(J)$ measures the sensitivity of the resulting vector field by measuring the strongest local stiffness or perturbation amplification along the trajectory. And because J contains M^{-1} it is tightly linked to the same near-singularity mechanism that drives the large condition number and small determinant.

A2.2.4 Wagner interaction parameters

It has also been observed that decreasing the Wagner interaction parameters of ε_{VC} (e) an ε_{MnC} (f) greatly decreases instability. Recalling the Schur-identity formulation for the mass-matrix:

(A2.6) $det(M) = det(B - vu^{T})$

Where:

$u \sim (ey_0(1 - y_0),\ fy_0(1 - y_0))$

$v \sim (ey_1(1 - y_1 - y_2),\ fy_2(1 - y_1 - y_2))$

Thus:

(A2.29) $$vu^T \sim \begin{pmatrix} e^2 & ef \\ ef & f^2 \end{pmatrix} * (\text{state-dependant factors})$$

Recalling the determinant analysis, if $|e|$ and $|f|$ are large, vu^T becomes large and can cancel B. When the Wagner interaction parameters become smaller, the only singularity mechanism left is the physical boundary, not internal cancellation. This is why reducing these parameters stabilises the system.

The same holds true for the condition number. When B is nearly canceled due to the large coupling, one singular value $\sigma_{min} \to 0$, but σ_{max} remains controlled. This leads to the condition number shooting up to high values.

And finally with the Jacobian, the Wagner interaction parameters are included in the inverse of the mass-matrix. If the interaction parameters make M near singular:

(A2.30) $$M^{-1} \sim \frac{1}{\sigma_{min}} \gg 1$$

In addition, they are included in the partial derivative of the mass-matrix, since:

$$g_1 = e y_0 (1 - y_0)$$
$$\frac{\partial g_1}{\partial y_0} \sim e(1 - 2y_0)$$

This means that derivatives of M scale with the interaction parameters.